J Adv Ceram

Research Article

Li/Mn co-doped $K_{0.5}Bi_{4.5}Ti_4O_{15}$ high-temperature piezoelectric ceramics: Structures, properties, and ultrasonic transducer applications

Junnan Wang, Zhi Zhou, Chengxin Xu, Jiageng Xu✉, Yu Chen✉

Cite this article: Wang J, Zhou Z, Xu C, et al. *J Adv Ceram* 2026, **15**(4): 9221277. https://doi.org/10.26599/JAC.2026.9221277

ABSTRACT: $K_{0.5}Bi_{4.5}Ti_4O_{15}$ (KBT, Curie temperature T_C = 558 °C), a representative Aurivillius-type ferroelectric material, is considered a promising candidate for high-temperature piezoelectric devices. In this study, the co-doping strategy was adopted by introducing Li/Mn ions into the A-site of KBT, and a series of polycrystalline ceramics with the formula $(KBi)_{0.5-x}(LiMn)_xBi_4Ti_4O_{15}$ (x = 0–0.065, abbreviated as KBT–LM1000x) were synthesized via the conventional solid-state reaction method. The substitution mechanisms of Li/Mn ions and their doping concentration effects on the crystalline structure, defect chemistry, and dielectric/ferroelectric properties were investigated. The synergistic substitution of Li/Mn for K/Bi induced a transition of KBT in its dielectric behavior from a sharp λ-type anomaly to a diffuse or relaxor-like response, with both diffuseness parameter γ and T_C values gradually increasing with increasing x. The Li/Mn co-doping strategy effectively suppressed the leakage conduction of KBT, achieving balanced control of conduction suppression and domain-wall mobility. Among the systems, KBM55 achieved the highest piezoelectric coefficient (d_{33} = 30 pC/N) and planar electromechanical coupling factor (k_p = 6.4%), as well as a higher Curie temperature (T_C = 590 °C). Furthermore, an ultrasonic transducer was fabricated by using this sample as conversion elements, which demonstrated a center frequency (f_c) of 2.24 MHz, a −6 dB bandwidth ($BW_{-6\,dB}$) of 33.95%, and stable pulse–echo signals up to 250 °C.

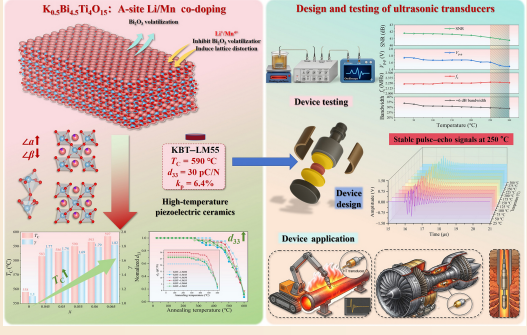

KEYWORDS: $K_{0.5}Bi_{4.5}Ti_4O_{15}$; Li/Mn co-doping; high-temperature stability; pulse–echo signal; ultrasonic transducer

1 Introduction

Ceramic materials, with their tunable electrical insulation, dielectric response, and polarization characteristics, have long been regarded as functional materials for energy conversion and sensing applications [1–5]. Among them, piezoelectric ceramics, owing to their strong electromechanical coupling, compact size, and high sensitivity, have been widely applied in ultrasonic transducers, energy harvesters, and high-temperature detectors [6]. With the expansion of application scenarios from ambient conditions to extreme environments, the demand for thermally stable piezoelectric ceramics has grown significantly. In harsh-environment scenarios such as downhole well logging and aerospace systems, ultrasonic transducers must sustain stable operation under high temperature/pressure, vibration, and aggressive conditions. Their practical temperature limit is often dictated not only by the Curie temperature but also by thermally activated conduction/loss and the thermal tolerance of bonding/interconnect materials. However, traditional lead-based ceramics such as lead zirconate titanate (PZT) and its derivatives, despite exhibiting excellent piezoelectric performance, face environmental issues and performance degradation in coupled thermo-electro-mechanical fields [7].

Aurivillius-phase compounds, also known as bismuth layered-structured ferroelectrics (BLSFs), are a class of layered perovskite-type oxides with the general formula $(Bi_2O_2)^{2+}(A_{m-1}B_mO_{3m+1})^{2-}$. These compounds are constructed from perovskite-like blocks interleaved with bismuth oxide layers $(Bi_2O_2)^{2+}$ [8–10]. To meet the demands of advanced industries, BLSFs with superior comprehensive properties have attracted increasing attention in recent years. However, within the BLSF system, certain materials still face challenges in achieving a balance between high Curie temperature T_C, large piezoelectric coefficient d_{33}, and ideal resistivity [11–15]. Among these materials, $K_{0.5}Bi_{4.5}Ti_4O_{15}$ stands out, having been first synthesized by Subbarao [16,17] in the 1960s. It was reported to be difficult to densify through conventional sintering, with the relative density reaching only approximately 85% of the theoretical value and a piezoelectric coefficient d_{33} as low as 10 pC/N.

Although $K_{0.5}Bi_{4.5}Ti_4O_{15}$ (KBT), as a representative bismuth-

School of Mechanical Engineering, Chengdu University, Chengdu 610106, China.

✉ Corresponding authors. E-mail: J. Xu, xujiageng@cdu.edu.cn; Y. Chen, chenyuer20023@163.com

Received: December 3, 2025; Revised: March 5, 2026; Accepted: March 5, 2026

layered piezoelectric ceramic, possesses the inherent advantages of Aurivillius-type structures, its piezoelectric performance and Curie temperature remain relatively low, and the synthesis process is challenging. In recent years, Wang *et al.* [18,19] successfully fabricated dense KBT ceramics with relative densities above 95% and achieved a d_{33} value of 21 pC/N. Furthermore, A-site Ce doping was shown to enhance the piezoelectric properties, with the maximum d_{33} reaching 28 pC/N in doped KBT ceramics. Similarly, Guo *et al.* [20] reported that Co-doping significantly improved the piezoelectric activity of KBT ceramics, yielding a d_{33} of 28 pC/N and a Curie temperature of 575 °C.

In this study, the KBT system was selected owing to its relatively high Curie temperature ($T_C \approx 558$ °C) and promising piezoelectric activity ($d_{33} > 20$ pC/N). Previous studies have demonstrated that introducing low-valence ions such as Li^+ together with transition-metal ions such as Mn at the A-site can effectively reduce the sintering temperature, suppress Bi volatilization, and regulate defect dipoles, thereby significantly enhancing structural integrity and electrical performance [21,22]. Therefore, in this work, Li/Mn ions with dodecahedral coordination were selected as dopants to occupy the pseudo-perovskite A-sites between the $(Bi_2O_2)^{2+}$ layers, with the aim of improving the piezoelectric performance of KBT ceramics. Li/Mn co-doped KBT ceramics were synthesized by the conventional solid-state reaction method, and their microstructure and electrical properties were systematically investigated. Furthermore, the feasibility of the optimized composition for high-temperature ultrasonic transducer applications was verified.

2 Materials and methods

2.1 Preparation method of KBT–LM piezoelectric ceramics

Ceramic samples with the nominal composition of $(KBi)_{0.5-x}(LiMn)_xBi_4Ti_4O_{15}$ (x = 0, 0.045, 0.050, 0.055, 0.060, and 0.065, abbreviated as KBT–LM1000x: KBT, KBT–LM45, KBT–LM50, KBT–LM55, KBT–LM60, and KBT–LM65, respectively) were fabricated via the conventional solid-state reaction method. The starting materials and their purities were as follows: Bi_2O_3 (99%), K_2CO_3 (99%), TiO_2 (99.8%), Li_2CO_3 (99%), and MnO_2 (99%). The raw powders were weighed according to the stoichiometric ratios and ball-milled with zirconia balls in ethanol for 12 h to ensure homogeneous mixing. The slurry was then dried at 80 °C for 8 h, followed by calcination at 800 °C for 3 h to promote the formation of the desired phase. The calcined powders were further milled in ethanol for another 12 h to achieve better homogeneity and particle refinement. Subsequently, an aqueous polyvinyl alcohol (PVA) solution with a concentration of 8 wt% (8 g PVA dissolved in 92 g deionized water) was used as a binder, and the powders were granulated and uniaxially pressed into disk-shaped pellets with a diameter of 10 mm. The green compacts were sintered at 1080–1150 °C for 3 h, followed by annealing at 800 °C for 3 h to obtain dense ceramics. After sintering, the ceramics were polished to form uniform thin sheets with a thickness of approximately 0.4 mm, and silver electrodes were coated on both sides of the ceramics for subsequent performance characterization.

2.2 Manufacturing method of KBT–LM55 ultrasonic transducers

In this study, an ultrasonic transducer was fabricated using KBT–LM55 ceramics with silver electrodes as the active transmitting and receiving medium. The transducer was designed with a typical three-layer configuration consisting of a matching layer, a piezoelectric layer, and a backing layer. Specifically, the matching layer was composed of an epoxy-alumina composite, the piezoelectric layer employed KBT–LM55 ceramics, and the backing layer was prepared from an epoxy-tungsten composite. The KBT–LM55 ceramic element had a thickness of 0.4 mm and a diameter of 9 mm. The transducer housing was made of cylindrical brass, and all components were engineered to withstand high-temperature environments.

2.3 Characterization methods

The crystalline phases of the sintered samples were analyzed using an X-ray diffractometer (XRD; DX-2700B, Dandong Haoyuan, China), and the diffraction patterns were refined via the Rietveld method using the GSAS-II software package. Based on the refinement data, the crystal structures were constructed and visualized with VESTA. The surface morphology of the samples was observed by a scanning electron microscope (SEM; Quanta FEG 250, FEI, USA). The valence electronic states of the ceramic powders were examined by an X-ray photoelectron spectrometer (XPS; Versa probe III, PHI, Japan).

The dielectric properties, including the temperature-dependent relative permittivity (ε_r) and dielectric loss tangent ($\tan\delta$), were measured using an impedance analyzer equipped with a high-temperature furnace (TH2838H, Tonghui Electronics, China). Alternating current (AC) impedance spectra were further recorded in the temperature range of 350–600 °C and the frequency range of 20 Hz–2 MHz. Prior to the piezoelectric measurements, the sintered samples were poled in a silicone oil bath under a direct current (DC) electric field of 13 kV/mm at 150 °C for 30 min. The samples were then aged at room temperature (RT) for 24 h to release any internal stress before testing. The quasi-static piezoelectric coefficient (d_{33}) of poled ceramics was measured using a piezoelectric constant tester (ZJ-6AN, Institute of Acoustics, Chinese Academy of Sciences, China).

Additionally, thermal depolarization experiments were performed following room-temperature calibration of the d_{33} values. The samples were annealed in a muffle furnace at various temperatures from room temperature to 600 °C with 25 °C intervals for 4 h each. After natural cooling to room temperature, the d_{33} values were remeasured. Ferroelectric hysteresis loops were obtained using a ferroelectric test system (FETS-2000, Beijing Yanhua Technology, China) at 150 °C and 1 Hz.

Ultrasonic pulse–echo measurements were conducted using a pulser/receiver system (DPR 300, JSR Ultrasonics, Imaginant, USA), with a steel plate serving as the reflector. The temporal evolution of the signal amplitude was recorded in the temperature range of 25–300 °C. The pulse–echo response tests were carried out in silicone oil, where the temperature was precisely controlled using a thermostatic magnetic stirrer with a heating function (DF-101s, Yuhua Instrument, China). To ensure measurement accuracy, the transducers were held at the set testing temperature for more than 10 min prior to data acquisition.

3 Results and discussion

Figure 1(a) shows the XRD patterns of KBT–LM1000x ceramics, where the main diffraction peaks of all samples match the primary phase of KBT ceramics, in accordance with the JCPDS 49-0608, indicating that ion substitution does not disrupt the layered structure of the parent phase. The most intense diffraction peak of all samples appears at the (119) plane, which is consistent with the crystallographic features of m = 4 Aurivillius-type ferroelectrics.

This result confirms that KBT is the primary phase within the 2θ range of 10°–90°. However, several small peaks are clearly observed, corresponding to the impurity phase $Bi_{1.74}Ti_2O_{6.624}$ (JCPDS 89-4732), and are marked with plum blossom symbols. Figure 1(b) presents the crystal structure of KBT–LM1000x ceramics, where K/Bi atoms occupy the interlayer sites and Ti atoms are located at the centers of TiO_6 octahedra.

To further investigate the crystal structure of KBT–LM1000x ceramics, two-phase Rietveld refinements were performed on the XRD patterns of all samples within the 2θ range of 10°–90°, using the crystal structures of $K_{0.5}Bi_{4.5}Ti_4O_{15}$ and $Bi_{1.74}Ti_2O_{6.624}$ extracted from their CIFs as structural models. The corresponding refinement profiles of the KBT–LM1000x ceramics are shown in Figs. 1(c)–1(h), while Table 1 presents the detailed refinement results for compositions with x = 0.00–0.065. A stable fitting quality, with a goodness of fit (GOF) value of approximately 1.62–1.93 and a weighted profile R-factor (R_{wp}) of approximately 3.13%–4.73%, was achieved through the "$K_{0.5}Bi_{4.5}Ti_4O_{15}$+ $Bi_{1.74}Ti_2O_{6.624}$" dual-phase refinement, indicating excellent agreement between the calculated and experimental patterns, thereby confirming the high accuracy of the structural model. All obtained reliability factors fall within acceptable ranges, validating the credibility and robustness of the refinement. As shown in Table 1, the $Bi_{1.74}Ti_2O_{6.624}$ impurity phase fraction decreases from 7.7% in pure KBT to 3.9% for KBT–LM45 and 3.1% for KBT–LM50, reaching a minimum of approximately 1.7% in KBT–LM55, and then slightly increases to approximately 5% for KBT–LM60 and KBT–LM65. The presence of the $Bi_{1.74}Ti_2O_{6.624}$ impurity phase may negatively affect the electrical properties of KBT ceramics, particularly their piezoelectric and dielectric performance. The KBT–LM55 sample exhibits the lowest impurity phase content, which contributes to enhanced structural stability. This, in turn, directly improves its electrical properties and mitigates performance degradation caused by oxygen vacancies and Bi volatilization. The $Bi_{1.74}Ti_2O_{6.624}$ phase content in Li/Mn co-doped KBT ceramics (sintered at 1080 °C) is lower than

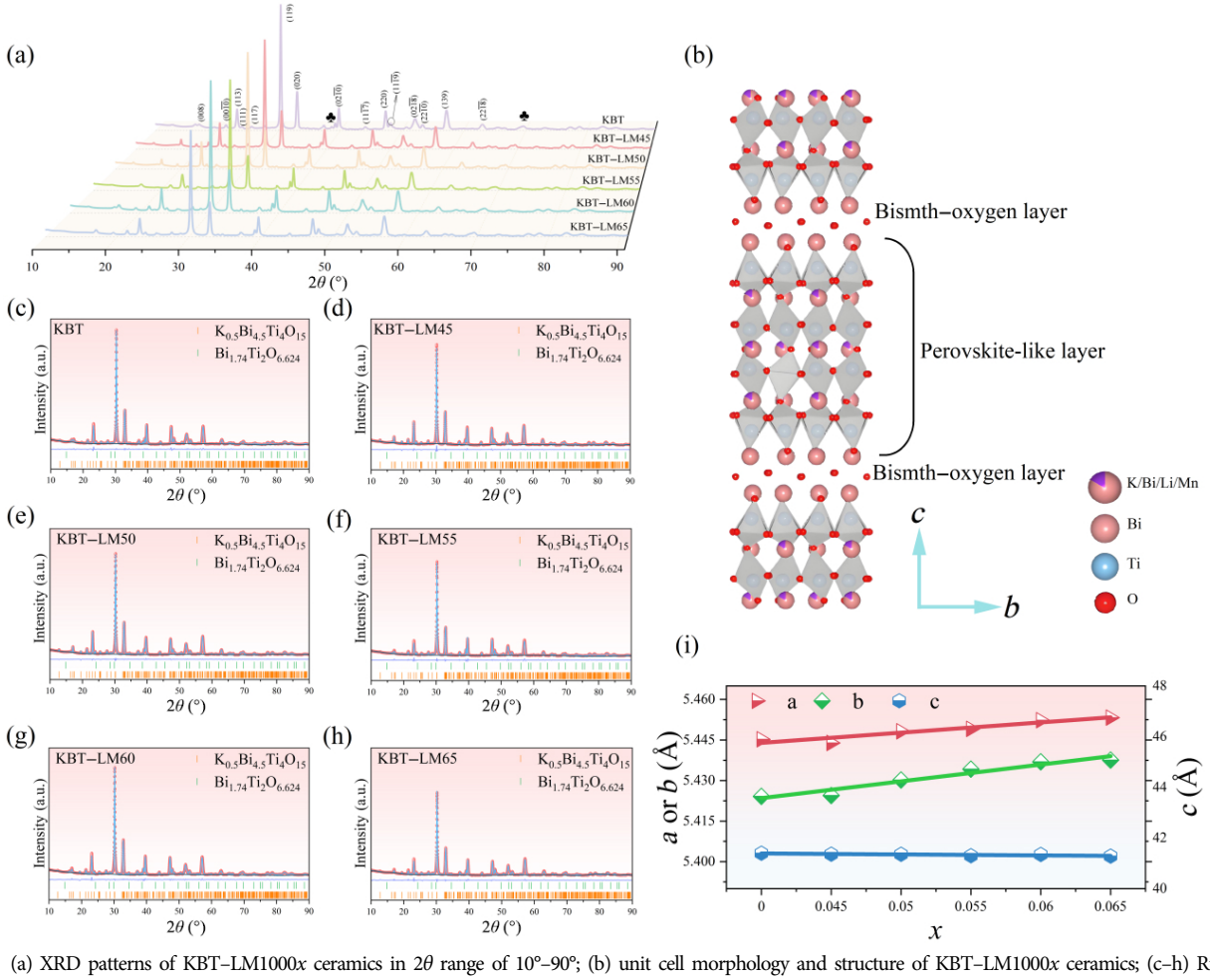

Fig. 1 (a) XRD patterns of KBT–LM1000x ceramics in 2θ range of 10°–90°; (b) unit cell morphology and structure of KBT–LM1000x ceramics; (c–h) Rietveld refinement results of KBT, KBT–LM45, KBT–LM50, KBT–LM55, KBT–LM60, and KBT–LM65 samples; (i) lattice parameters (a, b, and c) of KBT–LM1000x ceramics.

Table 1 Proportion of two phases and crystal structure parameters of KBT–LM1000x ceramics

	KBT	KBT–LM45	KBT–LM50	KBT–LM55	KBT–LM60	KBT–LM65
GOF	1.93	1.62	1.65	1.87	1.91	1.78
R_{wp} (%)	4.60	3.13	3.25	4.66	4.73	4.21
$K_{0.5}Bi_{4.5}Ti_4O_{15}$ (%)	92.3	96.1	96.9	98.3	95.0	94.9
$Bi_{1.74}Ti_2O_{6.624}$ (%)	7.7	3.9	3.1	1.7	5.0	5.1
a/b_{KBT}	1.00231	1.00358	1.00431	1.00574	1.00483	1.00388

that in pure KBT ceramics (sintered at 1150 °C). In previous studies of bismuth-layered ferroelectrics, the formation of $Bi_2Ti_2O_7$ at the early stages of thermal treatment has been observed, which is related to the relative stability of $Bi_2Ti_2O_7$ in the Bi_2O_3–TiO_2 system. During sintering, as the ambient temperature gradually increases, the $Bi_2Ti_2O_7$ phase begins to transform into the $K_{0.5}Bi_{4.5}Ti_4O_{15}$ phase. In this process, due to the volatilization of Bi ions, $Bi_2Ti_2O_7$ may partially convert into $Bi_{1.74}Ti_2O_{6.624}$, which is more difficult to transform into $K_{0.5}Bi_{4.5}Ti_4O_{15}$ because its Bi/Ti ratio is lower than that of $K_{0.5}Bi_{4.5}Ti_4O_{15}$ [23,24].

Based on the phase fraction results shown in Table 1, it can be inferred that an appropriate amount of Li/Mn co-doping lowers the effective sintering temperature and facilitates local liquid-phase formation, thereby suppressing Bi volatilization and the accumulation of associated oxygen vacancies during sintering. This process stabilizes the growth of the main KBT phase and significantly reduces the formation of the $Bi_{1.74}Ti_2O_{6.624}$ secondary phase. However, when the doping concentration becomes excessive, the solubility limit and grain-boundary segregation lead to local deviations from stoichiometry, re-triggering Bi–Ti secondary precipitation and consequently increasing the $Bi_{1.74}Ti_2O_{6.624}$ phase fraction again—consistent with the Rietveld refinement results [22]. From the comparison of refined lattice parameters (*a*, *b*, and *c*), slight variations in the unit cell constants and the *a*/*b* ratio indicate the occurrence of lattice strain induced by Li/Mn incorporation. Notably, the sample with x = 0.055 exhibits a relatively larger *a*/*b* ratio, indicating enhanced in-plane lattice anisotropy. Such anisotropic distortion can be elastically coupled to the out-of-plane direction, thereby modifying the interlayer strain state and strengthening the interaction between the perovskite slabs and the $[Bi_2O_2]^{2+}$ layers within this doping range. In addition, near the solubility limit, compositional fluctuations and residual stress synergistically amplify local distortion. As x increases further, the accumulated strain and defect distribution become partially averaged, resulting in a gradual relaxation of the *a*/*b* ratio [25].

In general, elemental substitution induces significant structural distortion within perovskite blocks composed of corner-sharing TiO_6 octahedra. In the crystal structure of $K_{0.5}Bi_{4.5}Ti_4O_{15}$, four TiO_6 octahedral layers are sandwiched between two $[Bi_2O_2]^{2+}$ layers, and the symmetric plane containing O1 is perpendicular to the *c*-axis. Due to the existence of glide planes along the *b*-axis and mirror planes along the *c*-axis, the P_s of $K_{0.5}Bi_{4.5}Ti_4O_{15}$ single crystals is oriented along the *a*-axis [26].

As shown in Fig. 2(a), the tilt angles (α) of TiO_6 octahedra relative to the *c*-axis in Li/Mn co-doped KBT ceramics (4.35°, 5.06°, 6.06°, 4.74°, and 3.77°) are all larger than that of the undoped sample (2.60°). This suggests that Li/Mn incorporation enhances octahedral tilting, thereby increasing P_s along the *a*-axis and reflecting greater distortion of Ti–O octahedra along the *c*-axis. Meanwhile, the displacement of oxygen atoms can be characterized by the rotation of the octahedral layers, where the rotational extent is denoted by $\angle\beta$ ($\angle$O–O′–O″). Here, β is the rotation angle of the TiO_6 octahedron around the *a*-axis within the *a*–*b* plane since the O–O′ linkage in the octahedron is parallel to the *a*-axis. The rotations of the outer octahedral layers are described by $\angle\beta_{O2}$ ($\angle$O2–O′2–O″2) and $\angle\beta_{O7}$ ($\angle$O7–O′7–O″7), while $\angle\beta_{O4}$ ($\angle$O4–O′4–O″4) and $\angle\beta_{O8}$ ($\angle$O8–O′8–O″8) correspond to the inner layers [22].

Figures 2(b)–2(d) display the octahedral rotations of KBT–LM1000x ceramics, and the corresponding $\angle\beta$ values are summarized in Table 2. As x increases, the rotation angles ($\angle\beta_{O2}$, $\angle\beta_{O7}$, $\angle\beta_{O4}$, $\angle\beta_{O8}$) first decrease and then slightly increase. Compared with KBT–LM00, the smaller $\angle\beta$ values of Li/Mn-doped samples indicate a larger polarization component along the *a*-axis, favoring the enhancement of P_s and implying higher crystallographic symmetry [27].

Moreover, the refined *a*/*b* ratio remains close to unity across the entire composition range, indicating an overall weak long-range orthorhombic distortion. Notably, *a*/*b* exhibits a non-monotonic evolution with x, suggesting that Li/Mn co-substitution induces a competing/redistributed distortion landscape rather than a simple symmetry enhancement. Meanwhile, the octahedral distortion angles show composition-

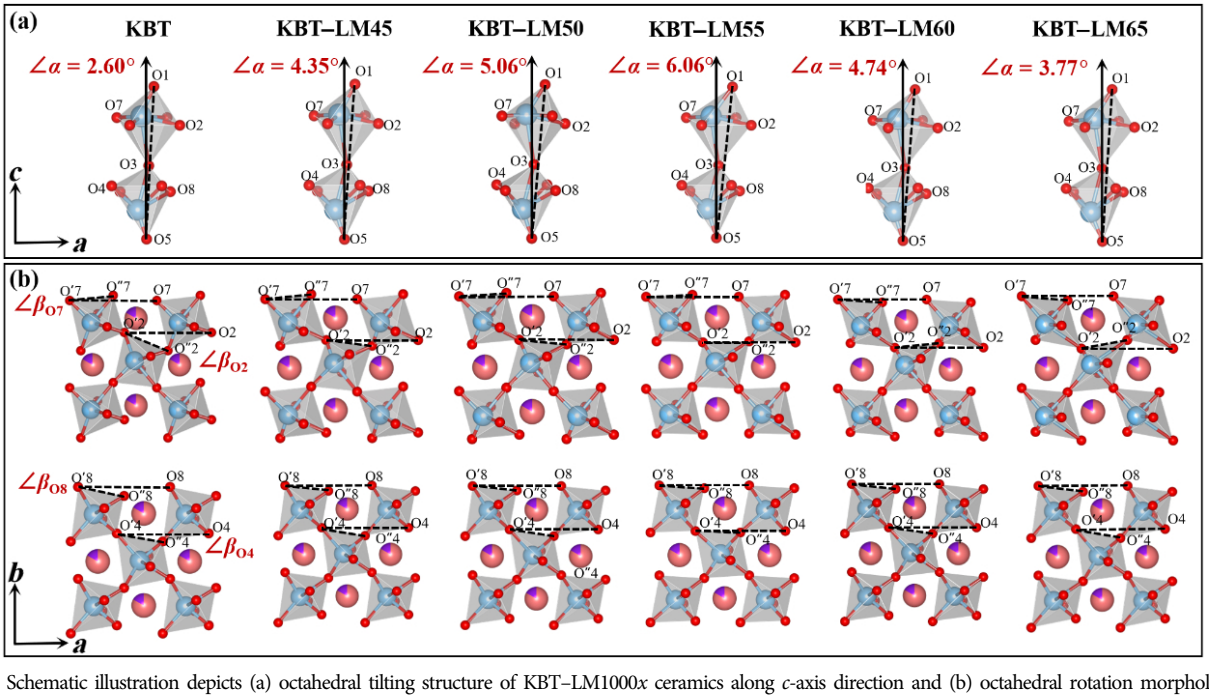

Fig. 2 Schematic illustration depicts (a) octahedral tilting structure of KBT–LM1000x ceramics along *c*-axis direction and (b) octahedral rotation morphology of KBT–LM1000x ceramics in *a*–*b* plane.

dependent rebalancing. Up to x = 0.055, α increases while β decreases, indicating a redistribution between tilt- and rotation-type distortions. With further increasing x, α relaxes, and β partially recovers, consistent with increased structural/compositional disorder and secondary-phase formation. In general, a higher average lattice symmetry reflects a suppressed long-range orthorhombicity, but it does not necessarily imply weakened local polar distortion. Instead, the field-induced response is largely controlled by domain switching and polarization rotation; their facilitated kinetics can enhance polarizability and electromechanical response while mitigating hysteresis and improving functional stability. In this context, the synergistic Li/Mn substitution reinforces local A–O electrostatic interactions and stabilizes the distorted framework. Together with the enhanced diffuseness parameter γ, these structural and chemical effects collectively account for the observed upward shift of T_C with increasing x.

Figures 3(a)–3(e) present the microstructural features of the KBT–LM1000x ceramics. In bismuth-layered structured compounds, grains oriented perpendicular to the c-axis generally exhibit higher growth rates during sintering, leading to pronounced crystallographic anisotropy and the formation of plate-like grains with irregular layered orientations. As shown in Fig. 3(a), the undoped KBT ceramics clearly display the plate-like morphology of the main phase $K_{0.5}Bi_{4.5}Ti_4O_{15}$ together with irregular particles of the $Bi_{1.74}Ti_2O_{6.624}$ impurity phase. Statistical comparison of the average grain lengths of the samples further reveals that Li/Mn co-doping effectively controlled the grain growth of KBT ceramics, resulting in a more homogeneous overall microstructure [22]. The incorporation of Li/Mn also reduced the sintering temperature of KBT ceramics from 1150 °C for the undoped composition to approximately 1080 °C for the doped samples. This decrease in the effective sintering temperature mitigated Bi volatilization, effectively suppressed the formation of impurity phases, and further optimized the grain morphology, resulting in a pronounced grain size refinement [28].

To further investigate the influence of Li/Mn co-doping on the valence state changes of B-site Ti^{4+} ions in KBT–LM1000x ceramics after substitution, XPS analysis was conducted on the KBT–LM1000x ceramics. As shown in Fig. 4, the survey spectra together with the high-resolution spectra of O 1s, Ti 2p, and Bi 4f were obtained for all samples. The corresponding fitted peak parameters, including binding energy, peak area, and relative area percentage, are summarized in Table 3. In the survey spectra, characteristic core-level peaks corresponding to Bi 4f, K 2p, Ti 2p, and O 1s were clearly observed, along with a minor C 1s signal originating from adventitious carbon.

Figure 4(b) presents the high-resolution O 1s spectra, which can be deconvoluted into three components centered at approximately 529.5 eV (O 1s (I)), 531.0 eV (O 1s (II)), and 532.5 eV (O 1s (III)), corresponding to lattice oxygen, non-lattice or defect-related oxygen environments, and surface-adsorbed oxygen species, respectively [29]. It should be emphasized that oxygen vacancies themselves do not directly contribute to an O 1s photoelectron peak; therefore, the relative peak areas obtained from O 1s deconvolution cannot be regarded as a quantitative measure of oxygen-vacancy concentration. Accordingly, the evolution of the O 1s (II) and O 1s (III) components is discussed here as a surface-sensitive indicator of defect-associated oxygen environments and adsorbed oxygen species, rather than a direct reflection of the absolute oxygen-vacancy population [30]. With A-site Li/Mn co-doping, cations with smaller ionic radii and distinct bonding characteristics compared with K/Bi are introduced into the lattice. Such substitution can locally modulate the A–O bond strength and alter the lattice distortion state around oxygen anions. This local structural relaxation may reduce the fraction of

Table 2 Octahedral rotation angles of KBT–LM1000x ceramics

	KBT	KBT–LM45	KBT–LM50	KBT–LM55	KBT–LM60	KBT–LM65
$\angle\beta_{O2}$	22.56	4.09	5.34	1.31	5.62	10.65
$\angle\beta_{O4}$	10.13	10.45	8.46	1.85	7.77	11.45
$\angle\beta_{O7}$	6.71	5.24	4.11	2.38	3.64	5.29
$\angle\beta_{O8}$	11.12	7.31	5.80	3.52	6.43	7.44

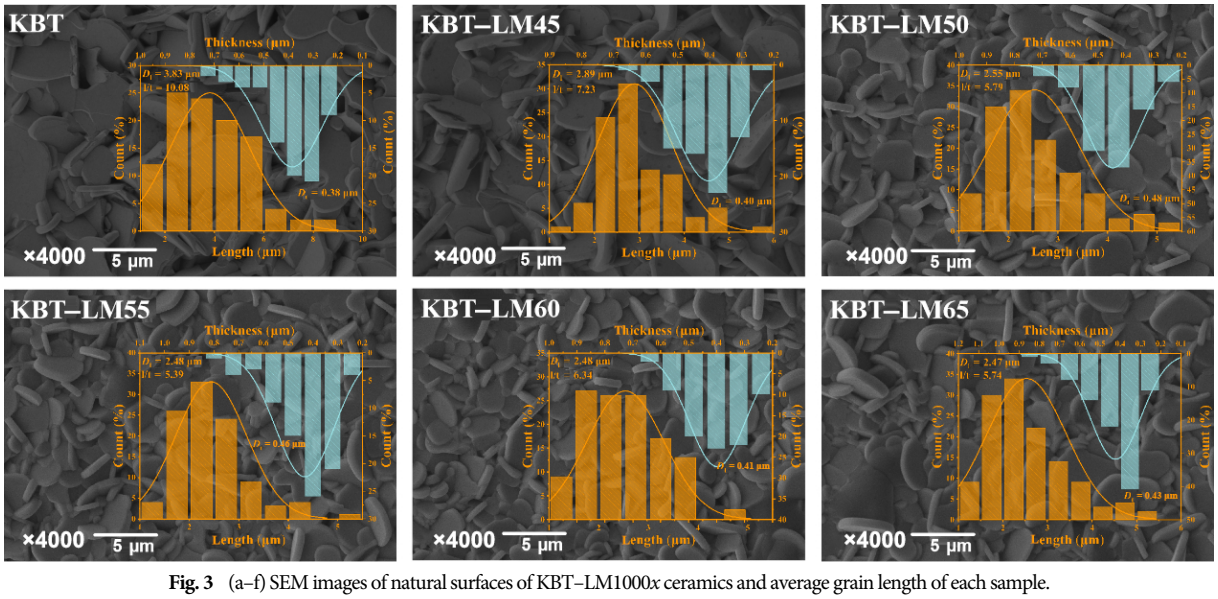

Fig. 3 (a–f) SEM images of natural surfaces of KBT–LM1000x ceramics and average grain length of each sample.

清華大学出版社 Tsinghua University Press | SciOpen

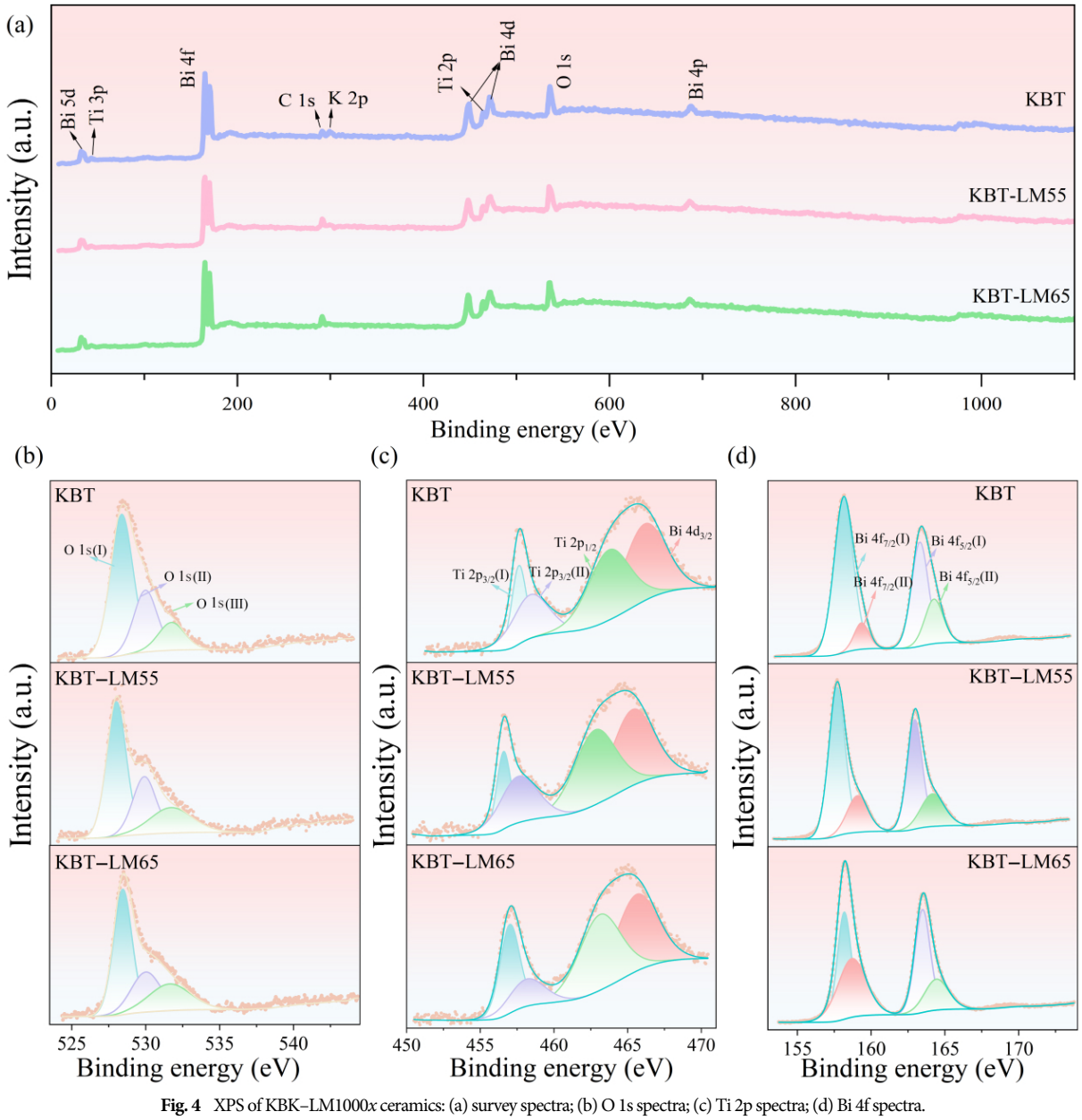

Fig. 4 XPS of KBK–LM1000*x* ceramics: (a) survey spectra; (b) O 1s spectra; (c) Ti 2p spectra; (d) Bi 4f spectra.

low-coordination or weakly bonded oxygen species, which are the primary contributors to the O 1s (II) signal. Therefore, the decrease in the relative proportion of the O 1s (II) component observed with increasing dopant content is more reasonably attributed to a redistribution of defect-related oxygen environments rather than to a direct increase in oxygen-vacancy concentration. This interpretation is consistent with the absence of a discernible Ti^{3+} component in the Ti 2p spectra and with the effective suppression of leakage conduction observed in the electrical measurements. Taken together with the markedly reduced dielectric loss and the significantly enhanced electrical resistivity at elevated temperatures, these results indicate that Li/Mn co-doping improves the material performance not merely by altering the oxygen-vacancy concentration but also by modulating the defect-chemical equilibrium and charge-transport pathways, thereby effectively suppressing leakage conduction and enhancing the insulation performance and high-temperature stability of the ceramics [31].

Figure 4(c) presents the high-resolution Ti 2p spectra of KBT–LM1000*x* ceramics. All compositions exhibit a clear spin–orbit doublet, with the Ti $2p_{3/2}$ and Ti $2p_{1/2}$ components located at approximately 457–458 and 463–464 eV, respectively, which is consistent with the characteristic binding energies of Ti^{4+} in Aurivillius-type titanates. In the range of 464–469 eV, the spectral envelope mainly arises from the overlap between the Ti $2p_{1/2}$ and Bi $4d_{3/2}$ signals. The Ti $2p_{3/2}$ main peak can be deconvoluted into two subcomponents; however, the energy separation between them is relatively small, and the overall line shape remains symmetric [32]. It is therefore more reasonable to ascribe these two components to subtle differences in the local coordination environment or microstrain of Ti^{4+} rather than to a well-resolved Ti^{4+}/Ti^{3+} mixed-valence state. No obvious low-binding-energy shoulder is observed for any composition, indicating that Ti ions predominantly remain in the +4 oxidation state after Li/Mn co-doping and that any Ti^{3+} is below the reliable detection limit of XPS. Consequently, the charge compensation associated with A-site co-substitution by low-valence Li/Mn ions is considered to be mainly achieved through the creation or annihilation of oxygen vacancies and A-site (K/Bi) vacancies, while the average Ti valence remains essentially unchanged [30].

From the viewpoint of defect chemistry, the introduction of low-valence Li/Mn ions at the A-site, partially substituting Bi^{3+}/K^+, disturbs the local charge balance, and the system compensates by generating oxygen vacancies and electrons to maintain charge neutrality. Taking Li_2CO_3 as an example, its decomposition during sintering and the subsequent incorporation of Li ions into the KBT lattice can be described by Reactions (1) and (2) [33–35]:

$$Li_2CO_3 \rightarrow Li_2O + CO_2 \quad (1)$$

$$Li_2O \rightarrow 2Li_{Bi}'' + 2V_O^{\cdot\cdot} + +O_O^{\times} \quad (2)$$

The oxygen vacancies ($V_O^{\cdot\cdot}$) generated in this process can, in principle, be involved in the reduction of Ti^{4+} to Ti^{3+}; a possible defect reaction can be written as Reaction (3):

$$Ti_{Ti}^{\times} + e' \rightarrow Ti_{Ti}' \quad (3)$$

For Mn, the valence state may vary among Mn^{2+}, Mn^{3+}, and Mn^{4+} depending on the local chemical environment, and its incorporation likewise requires charge compensation via oxygen vacancies and local charge rearrangement. In the present work, however, the Mn content is relatively low, and the characteristic XPS signals of different Mn valence states strongly overlap, making it difficult to extract reliable, species-resolved defect reactions [36]. Therefore, the role of Li/Mn co-doping is discussed at the level of overall defect equilibria, i.e., as a cooperative modulation of the oxygen-vacancy concentration and local charge distribution. Although a distinct Ti^{3+} component is not resolved in the Ti 2p spectra, the combined consideration of these defect reactions and the O 1s analysis suggests that A-site Li/Mn co-doping primarily tunes the oxygen-vacancy–related charge-compensation mechanism and the local coordination of TiO_6 octahedra, thereby indirectly influencing the conduction behavior and dielectric loss of the KBT–LM1000*x* ceramics [37]. The Bi 4f spectra in Fig. 4(d) show that the binding energies of all samples are consistent, corresponding to the typical Bi^{3+} oxidation state, with no evidence of metallic Bi^0, indicating that Bi maintains a stable valence state within the lattice structure.

3.1 Electrical characteristics

Figure 5 systematically illustrates the evolution of the high-temperature dielectric and piezoelectric properties of KBT–LM1000*x* ceramics as a function of the Li/Mn co-doping content. As shown in Fig. 5(a), all compositions exhibit a broad dielectric anomaly in the range of 550–600 °C, corresponding to the ferroelectric–paraelectric phase transition of the Aurivillius-type KBT matrix [38]. Compared with the undoped sample, Li/Mn co-doping leads to a slight decrease in the maximum permittivity, while the dielectric peak becomes markedly broadened with a flatter crest and an extended high-temperature tail, indicative of a typical dielectric dispersion behavior rather than a sharp λ-type transition [39]. This suggests that the T_C of the system is no longer concentrated at a single temperature point but is distributed over a finite temperature interval, so that the ferroelectric–paraelectric transition becomes partially "smeared out" and spatially nonuniform [40]. Meanwhile, the dielectric loss of the doped ceramics is significantly lower than that of pure KBT over the entire measured temperature range, and the peak value of tanδ near the phase transition is greatly reduced, indicating that Li/Mn co-doping effectively suppresses high-temperature conduction and space-charge polarization.

This suppression is primarily due to the modulation of the defect-chemical equilibrium within the Aurivillius structure. During the high-temperature sintering of KBT ceramics, the volatilization of Bi_2O_3 is unavoidable, which induces the formation of bismuth vacancies ($V_{Bi}^{'''}$) and oxygen vacancies ($V_O^{\cdot\cdot}$), as given by Reaction (4) [41]:

$$2Bi_{Bi}^{\times} + 3O_O^{\times} \rightarrow 2V_{Bi}^{'''} + 3V_O^{\cdot\cdot} + Bi_2O_3(g) \uparrow \quad (4)$$

The generated oxygen vacancies can further facilitate hole conduction at elevated temperatures through Reaction (5):

$$V_O^{\cdot\cdot} + \frac{1}{2}O_2 \rightarrow O_O^{\times} + 2h^{\cdot} \quad (5)$$

The substitution of low-valence Li ions into the A-site and the incorporation of multivalent Mn ions effectively counteract these intrinsic mobile carriers.

To quantitatively evaluate the degree of dielectric diffuseness, the modified Curie–Weiss law was employed in this work, as given by Eq. (6) [38]:

$$\frac{1}{\varepsilon_r} - \frac{1}{\varepsilon_{max}} = \frac{(T_r - T_{max})^{\gamma}}{C} \quad (6)$$

where ε_r is the relative permittivity at temperature T_r; ε_{max} is the

Table 3 XPS peak parameters of O 1s, Ti 2p, and Bi 4f of KBT–LM1000*x* ceramics

Test sample	Parameter composition	Pick binding energy (eV)	Area	Area (%)
KBT	O 1s (I)	528.75	18,118.74	58.1
	O 1s (II)	530.31	8885.46	28.5
	O 1s (III)	532.12	4178.21	13.4
	Ti $2p_{3/2}$ (I)	457.14	4305.81	12.7
	Ti $2p_{3/2}$ (II)	457.91	6114.10	18.1
	Ti $2p_{1/2}$	463.24	11,214.81	33.2
	Bi $4d_{3/2}$	465.65	12,186.91	36.0
	Bi$4f_{5/2}$ (I)	163.25	33,288.39	26.9
	Bi$4f_{5/2}$ (II)	164.16	18,728.30	15.2
	Bi $4f_{7/2}$ (I)	157.79	50,114.03	40.6
	Bi $4f_{7/2}$ (II)	158.76	21,439.51	17.4
KBT–LM55	O 1s (I)	528.39	14,075.92	52.3
	O 1s (II)	530.28	7153.70	26.6
	O 1s (III)	532.09	5688.38	21.1
	Ti $2p_{3/2}$ (I)	456.58	3907.88	11.6
	Ti $2p_{3/2}$ (II)	457.58	6562.79	19.4
	Ti $2p_{1/2}$	462.78	11,521.69	34.1
	Bi $4d_{3/2}$	465.32	11,777.93	34.9
	Bi$4f_{5/2}$ (I)	162.96	29,071.61	29.3
	Bi$4f_{5/2}$ (II)	164.17	13,615.58	13.7
	Bi $4f_{7/2}$ (I)	157.69	43,281.62	43.6
	Bi $4f_{7/2}$ (II)	159.08	13,385.70	13.5
KBT–LM65	O 1s (I)	528.85	13,497.29	50.2
	O 1s (II)	530.41	6890.28	25.6
	O 1s (III)	532.02	6505.70	24.2
	Ti $2p_{3/2}$ (I)	457.00	7922.42	19.2
	Ti $2p_{3/2}$ (II)	458.15	4446.13	10.8
	Ti $2p_{1/2}$	463.11	14,325.69	34.8
	Bi $4d_{3/2}$	465.59	14,483.31	35.2
	Bi$4f_{5/2}$ (I)	163.49	29,941.16	28.9
	Bi$4f_{5/2}$ (II)	164.43	14,104.65	13.6
	Bi $4f_{7/2}$ (I)	158.18	28,042.64	27.1
	Bi $4f_{7/2}$ (II)	158.70	31,419.56	30.4

maximum relative permittivity at the peak temperature T_{max}; γ is the diffuseness parameter indicating the degree of the diffuse phase transition; C is a Curie-like constant. By fitting the ε_r data on the high-temperature side ($T_r > T_{max}$) for each composition, the resulting diffuseness parameter γ was obtained and is plotted as a function of Li/Mn content x in Fig. 5(c). The diffuseness parameter γ increases markedly from approximately 1.10 for undoped KBT to approximately 1.8 upon the introduction of Li/Mn co-doping, indicating that the system evolves from a nearly classical sharp ferroelectric phase transition toward a distinctly diffuse or relaxor-like ferroelectric behavior. This evolution can be attributed to the combined effects of A-site Li/Mn co-doping-induced compositional disorder, local charge inhomogeneity, the presence of a small amount of $Bi_{1.74}Ti_2O_{6.624}$ impurity phase, and residual stress fields, all of which broaden the distribution of local phase-transition temperatures in different microregions. It is worth noting that γ exhibits a slight decrease at x = 0.055, implying a relatively weakened degree of diffuseness at this composition, which corresponds to a "structurally optimized" regime characterized by a more uniform grain size, the lowest $Bi_{1.74}Ti_2O_{6.624}$ impurity phase fraction, and a comparatively homogeneous defect configuration. When the doping level is further increased, γ increases again, suggesting that excessive Li/Mn co-doping enhances local disorder and random fields through increased impurity phase content, grain-boundary segregation, and defect accumulation, thereby intensifying dielectric diffuseness. These results demonstrate that the structural distortion parameters and γ evolve consistently with Li/Mn content, suggesting that the increased diffuseness is not governed by a single factor. Dopant-induced distortion redistribution together with enhanced A-site disorder can strengthen local random/stress fields and broaden the distribution of local transitions/responses, thereby increasing γ [42].

Figure 5(c) also depicts the evolution of T_C as a function of Li/Mn co-doping content x. It can be seen that T_C gradually increases from 558 °C for the undoped sample to 597 °C at x = 0.065, indicating that, while a certain degree of dielectric diffuseness is introduced, Li/Mn co-doping does not deteriorate the thermal stability of the ferroelectric phase in the KBT matrix; instead, it overall shifts the phase transition to higher temperatures. According to the Abrahams–Kurtz–Jamieson (AKJ) model, dopant-induced lattice distortion is expected to enhance spontaneous polarization and thus raise T_C [43].

In the present study, Rietveld refinement results show slight increases in the lattice parameters a, b, and c, with the structure maintaining a weak orthorhombic distortion across the entire doping range ($a/b \approx 1.002$–1.006). Notably, the sample with x = 0.055 exhibits the maximum deviation of a/b from unity, implying that in-plane lattice anisotropy is most pronounced at this composition [44]. In combination with the increase in the octahedral tilt angle α and the moderate adjustment of the rotation angle β, it can be inferred that an appropriate amount of Li/Mn co-doping simultaneously enhances the distortion of Ti–O bonds and the coupling between the $[Bi_2O_2]^{2+}$ layers and the perovskite-like blocks, thereby strengthening the spontaneous polarization and interlayer interaction and increasing the energy barrier for the ferroelectric–paraelectric phase transition, which drives the rise of T_C with increasing x.

However, when the doping level exceeds the optimal range (x > 0.055), T_C continues to rise despite local structural heterogeneity. This behavior can be attributed to the increasing effects of random fields and relaxor-like behavior. As the doping concentration increases, dielectric diffuseness broadens the phase transition, deviating from the sharp anomaly predicted by the AKJ model. High doping levels also induce local electric field inhomogeneities and defects, further enhancing dielectric dispersion and reducing overall ferroelectric stability [45].

To evaluate the effect of Li/Mn co-doping on the thermal

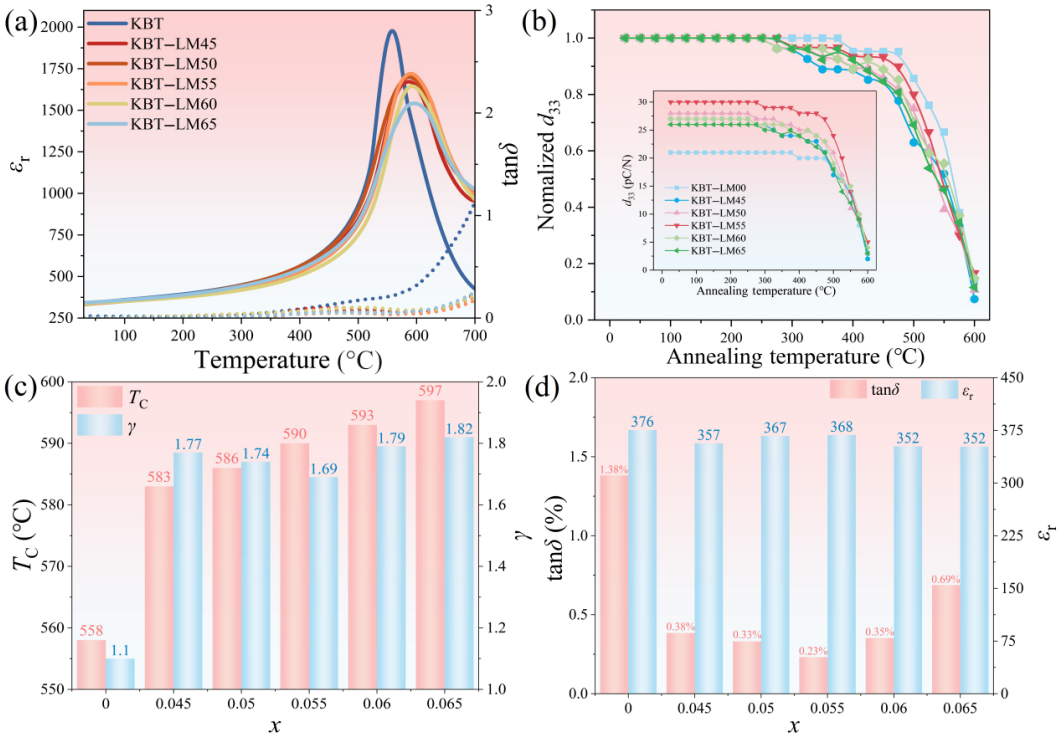

Fig. 5 (a) Temperature dependence of ε_r and tanδ for the KBT–LM1000x ceramics measured at 1 MHz; (b) normalized d_{33} as a function of annealing temperature for all KBT–LM1000x ceramics; inset shows unnormalized d_{33} as a function of annealing temperature; (c) evolution of T_C and γ as a function of Li/Mn co-doping level x in KBT–LM1000x ceramics; (d) composition-dependent ε_r and tanδ for KBT–LM1000x ceramics.

stability of the piezoelectric response, Fig. 5(b) presents the variation in the normalized d_{33} as a function of annealing temperature (the inset shows the corresponding d_{33} as a function of annealing temperature). For all compositions, the normalized d_{33} remains above 90% of its initial value below 400 °C, indicating good retention of polarization in the medium-temperature range for KBT-based Aurivillius ceramics. With a further increase in the annealing temperature, d_{33} gradually decreases and then drops sharply in the vicinity of the T_C. Among all samples, the KBT–LM55 composition exhibits the highest d_{33} retention, maintaining approximately 70%–80% of its initial value at 500 °C, which is significantly superior to both the undoped and the more heavily doped ceramics [46].

To further elucidate the relaxor-like dynamics and the thermal stability of polarization, the frequency dependence of the dielectric constant was analyzed using the Vogel–Fulcher (V–F) relationship (Eq. (7)) [47–49]:

$$f = f_0 \exp\left(\frac{-E_a}{k_B\,(T_m - T_f)}\right) \tag{7}$$

where f is the measuring frequency; f_0 is the pre-exponential factor (Debye frequency); E_a is the activation energy for dipole reorientation; k_B is the Boltzmann constant; T_m is the temperature of the maximum permittivity; T_f is the static freezing temperature. The fitting parameters for representative compositions are summarized in Table 4. As shown, the high correlation coefficients for the Li/Mn-doped samples confirm their typical relaxor-like behavior [50,51].

Interestingly, while the macroscopic T_C shifts to higher temperatures with increasing x, the calculated static freezing temperature T_f exhibits a sharp decline from 509.6 °C for pure KBT to 429.3 °C for KBT–LM55 and 361.8 °C for KBT–LM65. This decoupling indicates that the thermal stability of the piezoelectric response is primarily governed by T_f—the temperature at which polar nanoregions (PNRs) become dynamically frozen—rather than by the macroscopic phase transition temperature T_C. This provides a structural explanation for the observed decline in d_{33} in the 300–400 °C range, well below the peak T_C.

The enhanced relaxor behavior and depressed T_f are due to cation disorder caused by Li/Mn co-doping. Lightfoot *et al.* [52] suggested that A-site dopant substitution can cause misplacement between the perovskite blocks and $(Bi_2O_2)^{2+}$ layers, creating random electric fields that disrupt long-range ferroelectric order and lead to a broader distribution of local transition temperatures and frequency dispersion.

It is worth noting that KBT–LM55 also shows the lowest γ among the Li/Mn co-doped compositions, implying a relatively moderate level of dielectric diffuseness. This suggests that at x = 0.055, the microstructural and defect configurations reach a more balanced state: On the one hand, Li/Mn co-doping is sufficient to suppress high-temperature conduction and space-charge polarization, thereby reducing dielectric loss; on the other hand, the degree of disorder and random fields is not excessive, so that domain-wall motion is not severely pinned and a large fraction of the polarization remains switchable at elevated temperatures. As a result, KBT–LM55 achieves an optimal compromise between defect-mediated conduction suppression and domain mobility, leading to the best thermal stability of d_{33} within the investigated KBT–LM1000x ceramics. Figure 5(d) summarizes the relative permittivity at 150 °C and the dielectric loss at RT for KBT–LM1000x ceramics. The Li/Mn co-doped compositions exhibit slightly enhanced ε_r at 150 °C together with markedly reduced tanδ at RT compared with undoped KBT, and the co-doping strategy maintains high polarization while suppressing conduction losses at elevated temperatures.

Table 4 Dielectric diffuseness and Vogel–Fulcher parameters of representative KBT–LM1000x ceramics

	γ	T_C (°C)	T_f (°C)	E_a (eV)
KBT	1.1	558	509.6	0.067
KBT–LM55	1.69	590	429.3	0.226
KBT–LM65	1.82	597	361.8	0.328

Previous studies have revealed that the incorporation of an appropriate amount of Li/Mn ions contributes to a more uniform grain size distribution. Such a homogeneous microstructure reduces the hindrance of grain boundaries to domain growth, enabling ferroelectric domains to develop and align more effectively while mitigating domain-wall pinning [22]. Consequently, as shown in Fig. 6, a pronounced increase in remanent polarization (P_r) is observed, accompanied by an enhancement in d_{33}. Additionally, for a coordination number of 12, the ionic radii of Li^+ (1.25 Å), Mn^{3+} (1.03 Å) and Mn^{4+} (0.95 Å) are all smaller than those of K^+ (1.64 Å) and Bi^{3+} (1.45 Å) [53]. For Mn, although its actual oxidation state may vary with the sintering atmosphere and defect-compensation mechanisms, an upper-bound estimate of its A-site effective size can be obtained by using CN = 12 radii, as extrapolated by Xi *et al.* [22]. It should be emphasized that these Mn radii are introduced only for qualitative comparison and upper-bound estimation, rather than for quantitative assignment of the Mn valence state. Accordingly, the tolerance-factor-related discussion is intended only to qualitatively describe the structural tendency (chemical pressure) induced by A-site substitution. Overall, the partial substitution of Li/Mn at the A-site is expected to impose a local compressive stress on the lattice, and this structural effect can be reflected by the tolerance factor, as shown in Eq. (8) [54]:

$$t(x) = \frac{r_A + r_O}{\sqrt{2}\,(r_B + r_O)} \tag{8}$$

where $t(x)$ is the Goldschmidt tolerance factor, and r_A, r_B, and r_O are the average ionic radii of the A-site cations, B-site cations, and oxygen anions, respectively. As x decreases, the reduction in the average A-site ionic radius (r_A) results in a lower tolerance factor (t). To maintain coordination stability, the Ti–O octahedra undergo increased tilting or rotation, which typically manifests as a slight contraction of the a/b lattice parameters, a larger octahedral tilt angle, and a corresponding adjustment of the interlayer c-axis. In Aurivillius structures, such tilting often couples with polarization-related displacements, thereby potentially raising the intrinsic upper limit of P_s. At the same time, appropriate doping produces more uniform grains and fewer defects, which facilitates domain-wall mobility and increases the number of switchable domains under an external electric field. Consequently, the measured remanent P_r shows a noticeable enhancement [55]. When excessive doping is introduced, the increased formation of impurity phases tends to pin the domain walls and induce leakage currents. As a result, even though the upper limit of P_s remains unchanged, the fraction of domains that can be switched and retained is reduced, leading to a decrease in the remanent polarization [56]. Such behavior has also been observed in $Na_{0.5}Bi_{4.5}Ti_4O_{15}$-based Aurivillius ceramics [22]. Nevertheless, the stress and electric-field concentration induced by impurity phases at lattice defects strongly pin the domain walls. Thus, the defects and grain-boundary impurity phases generated by excessive doping collectively restrict the mobility of

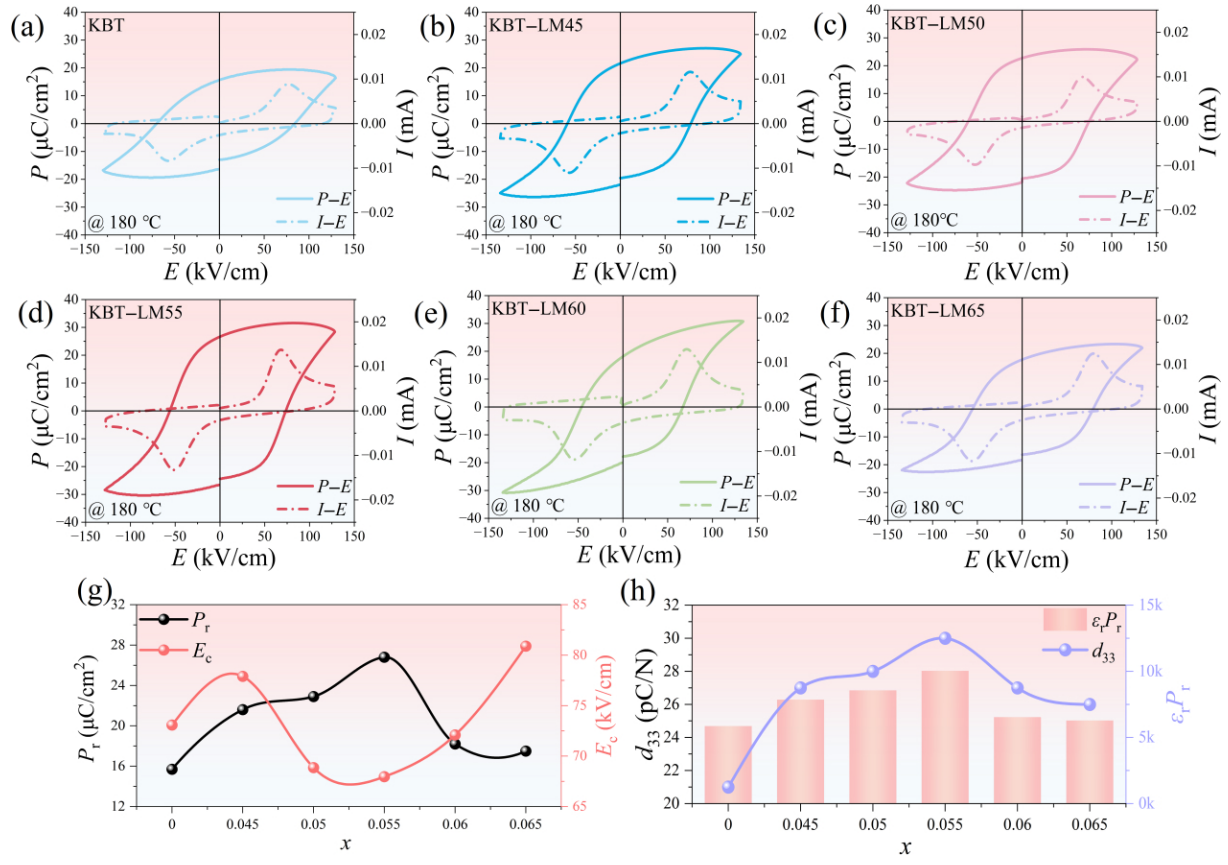

Fig. 6 (a–f) *P*–*E* and *I*–*E* loops for KBT–LM1000*x* ceramics; (g) P_r and E_c of KBT–LM1000*x* ceramics; (h) d_{33} and $\varepsilon_r P_r$ of KBT–LM1000*x* ceramics.

ferroelectric domains, driving the material from a ferroelectric state with highly mobile domain walls to one where their motion is severely constrained [57–59]. The variation in the piezoelectric coefficient d_{33} (calculated as $d_{33} = 2Q\varepsilon_r P_r$, where Q is the electrostriction coefficient) follows the same trend as that of $\varepsilon_r P_r$ shown in Fig. 6(h), further confirming the underlying reason for the change in d_{33}. This domain-wall pinning effect becomes more pronounced in heavily doped samples, which explains the decrease in P_r and d_{33} and the simultaneous increase in E_c observed in Fig. 6(g) when x is excessively large.

As an essential technique for probing dielectric and conduction characteristics, AC impedance spectroscopy enables an effective distinction between the contributions of grains and grain boundaries to charge transport while also providing insights into microscopic mechanisms such as defect states and ion migration. On this basis, systematic AC impedance measurements and analyses were conducted for KBT–LM1000*x* ceramics in the temperature range of 450–600 °C, including Nyquist plot features, the frequency dependence of conductivity, and the Arrhenius relationship of $\ln\sigma_{ac}$–1000/T, to elucidate the regulatory effect of Li/Mn A-site doping on the electrical transport behavior.

As shown in Fig. 7(a), all samples exhibit a well-defined single semicircular arc, indicating that in this temperature range, the conduction behavior is predominantly governed by the grain interiors, while the contributions from grain boundaries or electrode interfaces are negligible. This observation suggests that charge carriers mainly migrate within the grains under the studied conditions [60]. With increasing temperature, the radius of the semicircular arc gradually decreases, reflecting a reduction in resistance and, consequently, an enhancement in electrical conductivity. At lower temperatures (450 °C), the impedance response of all samples approaches the *y*-axis, indicating that KBT–LM1000*x* ceramics maintain high insulating properties at low temperatures. Further analysis reveals significant differences among samples with varying doping levels. In particular, the KBT–LM55 composition exhibits the largest arc radius in the Nyquist plot, suggesting a relatively higher AC impedance and stronger suppression of charge transport, thereby demonstrating superior insulating characteristics. In addition, the non-ideal circular shape of the Nyquist arc suggests a non-Debye-type relaxation process. The slight flattening of the semicircular contour further indicates the presence of non-Debye relaxation characteristics, which is consistent with oxygen-vacancy-related relaxation mechanisms common in Aurivillius-type layered ceramics.

As shown in Fig. 7(b), the AC conductivity ($\ln\sigma_{ac}$–*f*) further reveals the conduction processes at different frequencies. In the low-frequency region, $\ln\sigma_{ac}$ remains nearly constant, corresponding to the contribution of DC conductivity, whereas in the high-frequency region, $\ln\sigma_{ac}$ of all compositions increases sharply, indicative of typical polaron-hopping conduction behavior. With increasing temperature, the overall $\ln\sigma_{ac}$ curves shift upward, reflecting a thermally activated conduction mechanism. The Arrhenius fitting results in Fig. 7(c) demonstrate that the activation energies for conduction (E_a^{con}) of different samples vary significantly, with KBT–LM55 and KBT–LM50 reaching 1.243 and 1.217 eV, respectively, which are notably higher than those of KBT–LM00 (0.945 eV) and KBT–LM65 (0.872 eV). This indicates that appropriate doping can effectively raise the migration barrier of charge carriers, thereby suppressing the leakage current and enhancing the high-temperature insulation performance.

Figure 8(a) shows the resonance–antiresonance spectra of KBT–LM55 ceramics measured at different temperatures. As the temperature increases, both the resonance and antiresonance peaks gradually shift toward lower frequencies, indicating an

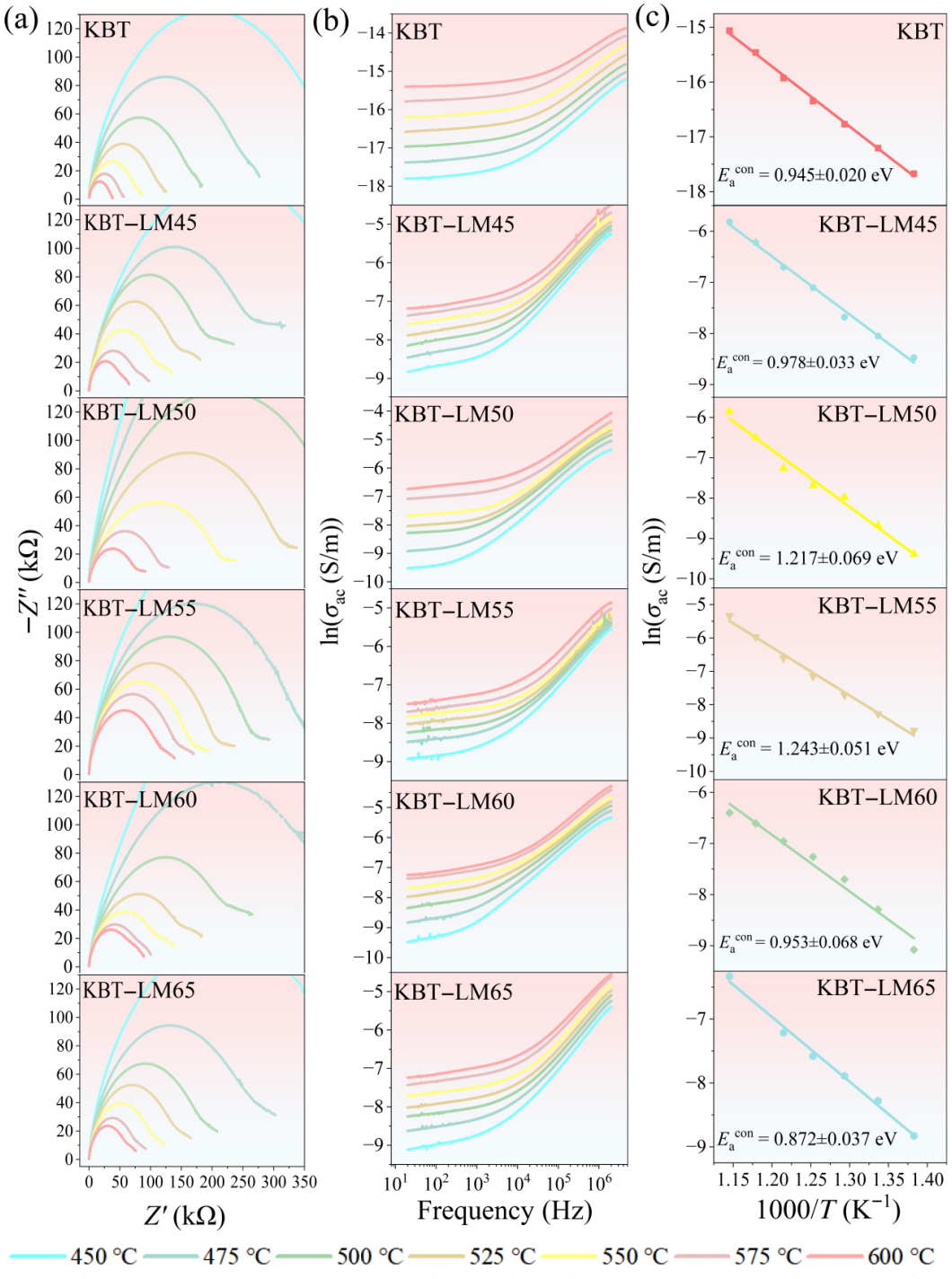

Fig. 7 (a) Nyquist plots of KBT–LM1000*x* ceramics measured in range of 450–600 °C; (b) frequency-dependent AC conductivity spectra of samples at different temperatures; (c) Arrhenius plots of lnσ_{ac} versus 1000/T for samples.

elastic softening behavior of the material. The inset presents the temperature dependence of the planar frequency constant (N_p), which exhibits an approximately linear decrease over a wide temperature range, demonstrating excellent thermal stability of the resonance frequency. When the temperature rises further, the resonance–antiresonance pair becomes less distinguishable, suggesting the occurrence of thermal depoling and the degradation of long-range ferroelectric ordering [61].

Similar to other Aurivillius-type ceramics, the impedance amplitude (|Z|) of the Li/Mn co-doped KBT ceramics progressively decreases with increasing temperature, mainly due to the enhanced electrical conductivity at elevated temperatures. Under these conditions, the equivalent circuit used to extract piezoelectric parameters such as the planar electromechanical coupling factor (k_p) and the mechanical quality factor (Q_m) may no longer be strictly applicable. Nevertheless, N_p, which depends solely on the resonance frequency, remains a reliable indicator of the intrinsic thermal stability [62].

As shown in Fig. 8(b), k_p exhibits a relatively stable variation with temperature, indicating that the piezoelectric coupling remains well preserved within the measured range. In contrast, Q_m gradually decreases with increasing temperature, which can be attributed to enhanced domain-wall damping and thermally activated charge-conduction losses. Overall, the KBT–LM55

ceramics exhibit excellent piezoelectric stability and favorable mechanical quality at elevated temperatures, confirming their potential for high-temperature piezoelectric applications.

To further directly evaluate the temperature-activated conduction, Fig. 8(c) presents the temperature dependence of DC resistivity ρ_{dc} for KBT–LM1000x ceramics. All compositions exhibit a pronounced decrease in ρ_{dc} with increasing temperature, confirming the thermally activated transport behavior. Importantly, the Li/Mn co-doped samples maintain an overall higher ρ_{dc} than the KBT over a broad temperature range, indicating that co-doping effectively suppresses high-temperature leakage conduction and improves insulation performance. This DC-resistivity evidence provides more straightforward support for the reduced high-temperature loss and conduction inferred from the dielectric and impedance analyses, and it is directly relevant to stabilizing the piezoelectric response under elevated-temperature operation.

3.2 Design of ultrasonic transducers

To further investigate the thermal stability and device applicability of KBT–LM1000x ceramics, an ultrasonic transducer was designed and fabricated using the KBT–LM55 sample, which exhibited the optimal overall performance. The acoustic characteristics of the fabricated transducer were systematically tested and analyzed. As illustrated in Fig. 9(c), the transducer adopts a typical layered configuration consisting of a matching layer, a piezoelectric layer, and a backing layer. The matching layer, composed of an epoxy/alumina composite, serves to achieve a smooth acoustic impedance transition from the surrounding medium to the piezoelectric element. The backing layer, made of an epoxy/tungsten composite, provides strong acoustic attenuation to absorb backward-propagating waves and suppress ringing effects. The core piezoelectric layer is a thin KBT–LM55 ceramic plate, functioning as both the transmitting and receiving unit of the transducer. The pulse–echo measurements of the fabricated device were performed using the experimental setup shown in Fig. 9(a).

The pulse–echo responses of KBT–LM1000x ceramics at different temperatures (from RT to 300 °C) were measured in a confined heating environment and are presented in Fig. 10. Figure 10 shows the measured pulse–echo waveforms and corresponding frequency spectra obtained through fast Fourier transform (FFT) at temperatures ranging from room temperature to 300 °C. The peak-to-peak values (V_{p-p}), center frequency (f_c), −6 dB bandwidth ($BW_{-6\,dB}$), and signal-to-noise ratio (SNR) were calculated using Eqs. (9)–(12) [63]:

$$V_{p\text{-}p} = V_+ + V_- \tag{9}$$

$$f_c = \frac{f_{lower} + f_{upper}}{2} \tag{10}$$

$$BW = \frac{f_{lower} + f_{upper}}{f_c} \times 100\% \tag{11}$$

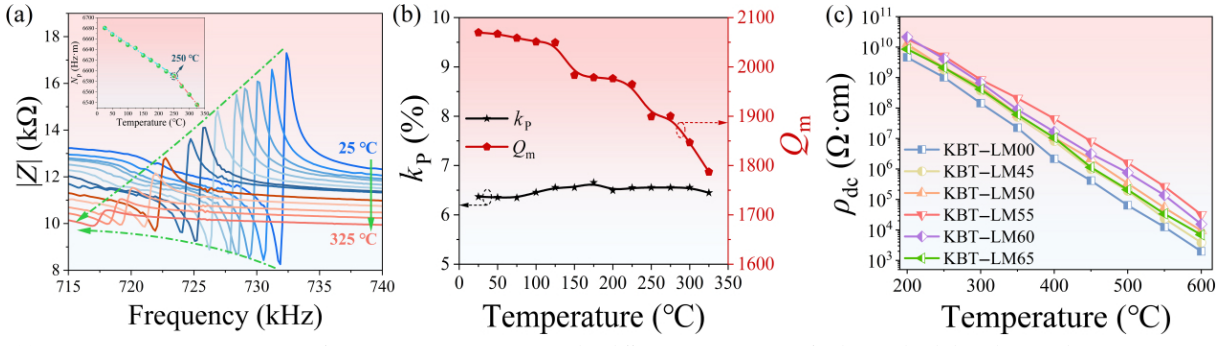

Fig. 8 (a) Resonance–antiresonance spectra of KBT–LM55 ceramics measured at different temperatures in fundamental radial mode; inset shows variation in N_p with temperature; (b) temperature dependence of k_p and Q_m; (c) temperature dependence of DC resistivity of KBT–LM1000x.

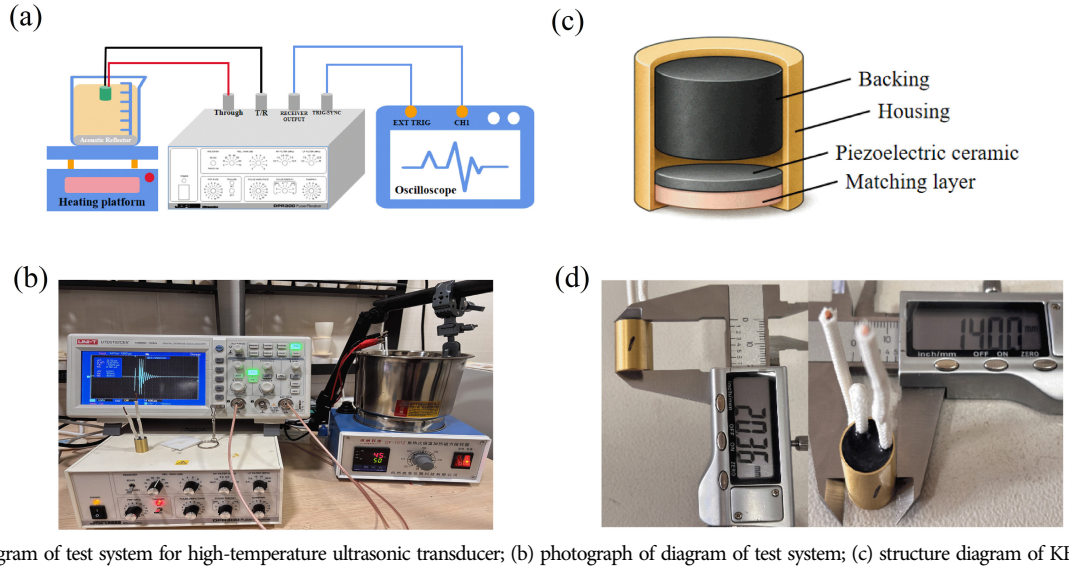

Fig. 9 (a) Diagram of test system for high-temperature ultrasonic transducer; (b) photograph of diagram of test system; (c) structure diagram of KBT–LM55 high-temperature ultrasonic transducer; (d) photograph of KBT–LM55 high-temperature ultrasonic transducer.

$$\mathrm{SNR\ (dB)} = 10\log\frac{V_{\mathrm{signal}}}{V_{\mathrm{noise}}} \tag{12}$$

where f_{lower} and f_{upper} are the frequency values corresponding to the −6 dB points of the high-frequency and low-frequency intersections on the signal spectrum, respectively; V_{signal} is the effective amplitude of the echo signal; V_{noise} is the effective amplitude of the background noise. $V_{\mathrm{P\text{-}P}}$ is the peak-to-peak voltage of the ultrasonic echo signal, and V_+ and V_- represent the maximum positive amplitude and the absolute value of the maximum negative amplitude, respectively. As shown in Fig. 11(a), experimental measurements and calculations reveal that at room temperature, the sensor exhibits an f_c of 2.24 MHz, a $BW_{-6\ dB}$ of 28.58%, a V_{p-p} of 1.94 V, and an SNR of 29.8 dB. With increasing temperature, the V_{p-p} of the echo signal shows a slight attenuation at 250 °C, while both SNR and $BW_{-6\ dB}$ display a downward trend; nevertheless, the f_c remains essentially stable

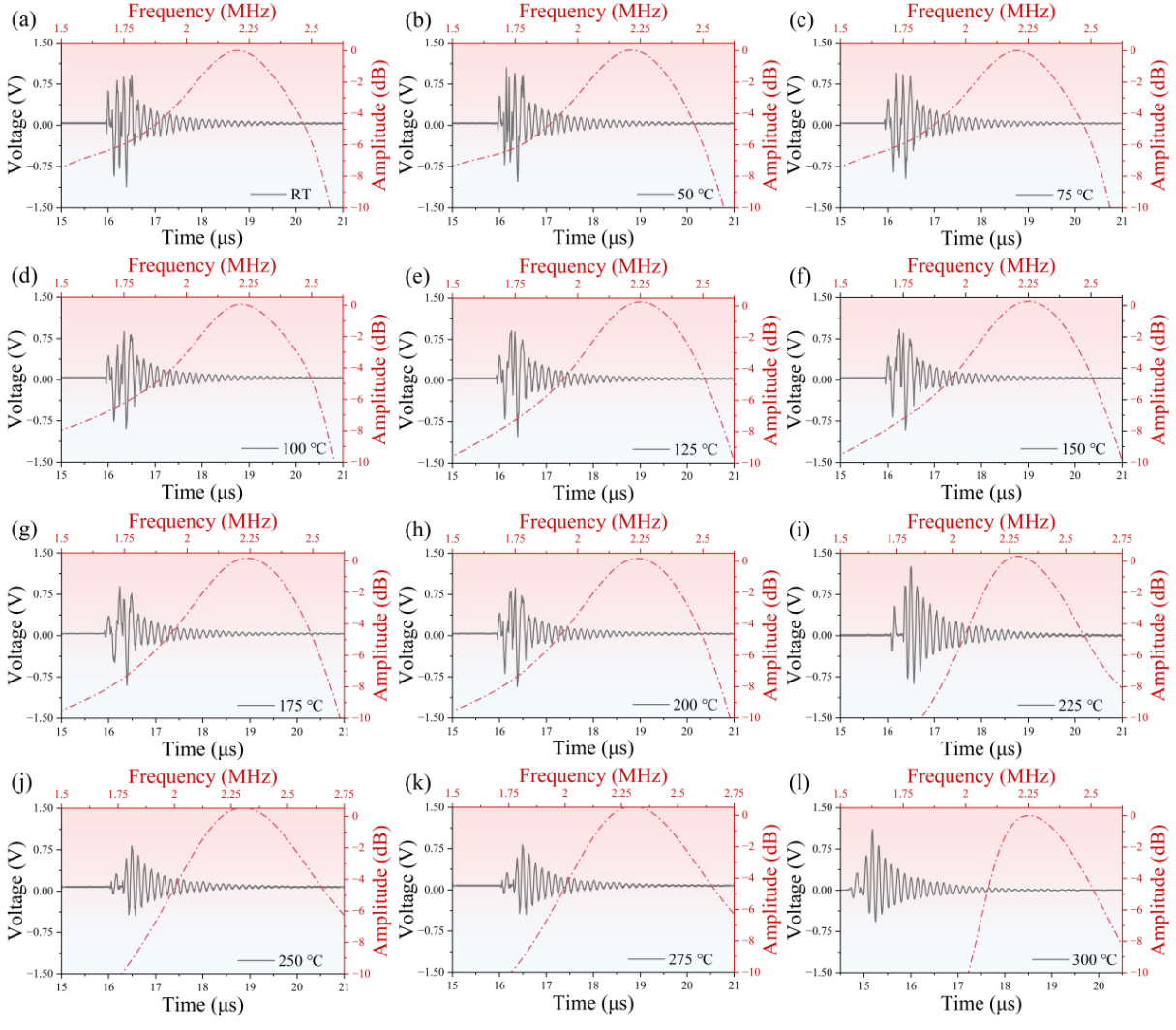

Fig. 10 Measured pulse–echo waveform and frequency spectra of KBT–LM55 ultrasonic transducer measured at various temperatures.

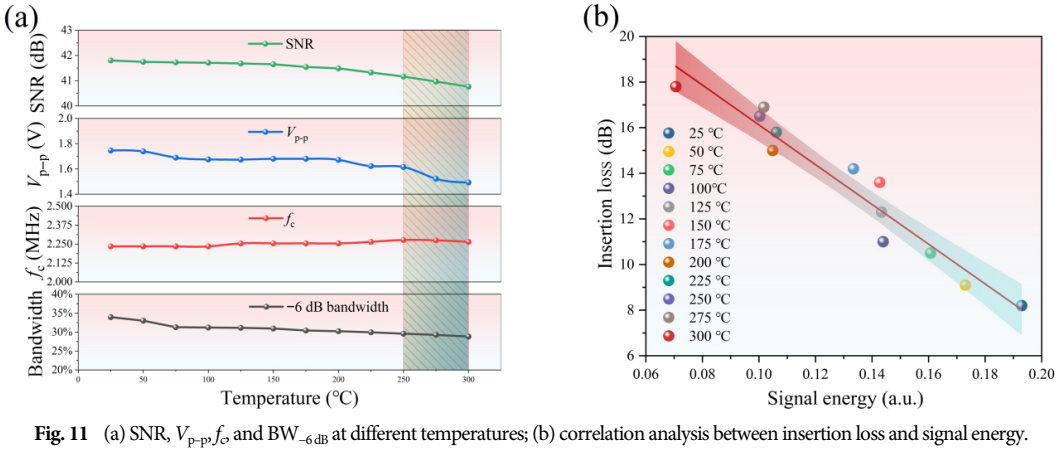

Fig. 11 (a) SNR, V_{p-p}, f_c, and $BW_{-6\ dB}$ at different temperatures; (b) correlation analysis between insertion loss and signal energy.

without noticeable fluctuations. This phenomenon may be attributed to the decrease in the acoustic impedance of silicone oil with rising temperature, which intensifies the mismatch with the load impedance and simultaneously causes a shift in matching conditions and acoustic parameters. As a result, the system exhibits larger energy loss at the medium-transducer interface, leading to reduced effective energy transfer and attenuation of the echo amplitude, while the propagation of the ultrasonic wave excited by the transducer undergoes increased energy dissipation.

Insertion loss (IL) and signal energy are also key parameters for evaluating the performance of ultrasonic transducers, where the calculation of IL is given by Eq. (13) [64]:

$$\mathrm{IL\ (dB)} = 20\log\frac{V_t}{V_r} \tag{13}$$

where V_t is the transmitting voltage and V_r is the received echo voltage. The signal energy (E) can be approximated as the integral of the squared echo voltage (Eq. (14)):

$$E = \int v^2(t)\,\mathrm{d}t \tag{14}$$

where E represents the total signal energy of the ultrasonic echo, $v(t)$ is the instantaneous voltage of the received echo as a function of time. As Eq. (14) reveals, a larger energy corresponds to a higher echo voltage. Accordingly, the calculation of IL can be reformulated as Eq. (15):

$$\mathrm{IL\ (dB)} = 20\log\frac{V_t}{k\sqrt{E}} \tag{15}$$

where k is a proportional constant, and after simplification, Eq. (15) can be interpreted as indicating a linear relationship between insertion loss and signal energy [65]. As shown in Fig. 11(b), IL exhibits a pronounced negative linear correlation with the echo signal energy. With increasing signal energy, IL decreases at a approximately constant rate, suggesting that energy attenuation is one of the dominant factors governing system losses. The color mapping further reveals that high-temperature data points are mainly distributed in the low-energy, high-loss region, reflecting that the elevated temperature induces increased internal damping of the material and simultaneous degradation of the acoustic parameters of the coupling medium and matching layer, thereby leading to additional energy dissipation.

In addition, as can be observed from the thermal depoling behavior of KBT–LM1000x ceramics shown in Fig. 5(b), the poled KBT–LM1000x ceramics were annealed at elevated temperatures with a soaking time of 1 h. Below 400 °C, the piezoelectric coefficient remains almost unchanged (only decreasing by approximately 10%). These results indicate that the Li/Mn co-doped KBT ceramics exhibit excellent thermal annealing resistance. Notably, the depoling resistance is evaluated after cooling to room temperature, and therefore, it cannot fully capture potential reversible changes in domain-wall dynamics or partial depolarization under *in situ* high-temperature operation. Nevertheless, the good retention of d_{33} after thermal exposure suggests that intrinsic domain instability is unlikely to be the sole or dominant origin of the performance fluctuation observed for the ultrasonic transducer at elevated temperatures. Such fluctuations are more plausibly associated with reversible temperature-dependent extrinsic factors, e.g., changes in the acoustic properties of the coupling medium, impedance matching conditions, interfacial bonding/damping, and thermally enhanced losses in the measurement environment. Furthermore, as seen from the resonance and antiresonance impedance spectra in Fig. 7, with increasing temperature, the resonance peaks of KBT–LM55 ceramics gradually broaden, and the impedance difference decreases; this, in turn, results in weakened energy concentration and retention capabilities of the device [66].

It is worth noting that although elevated temperatures induce a certain degree of performance degradation in the KBT–LM55 ultrasonic transducer, the KBT–LM55 device is still capable of producing a distinct echo signal at 300 °C, with both the center frequency and bandwidth maintained within an acceptable range. This result clearly demonstrates that Li/Mn co-doping not only enhances the room-temperature properties of KBT ceramics but also significantly improves their high-temperature stability, thereby enabling the potential application of such materials in extreme service environments.

4 Conclusions

$(KBi)_{0.5-x}(LiMn)_xBi_4Ti_4O_{15}$ (KBT–LM1000x, x = 0–0.065) ceramics were synthesized by the conventional solid-state reaction method, and the influence of Li/Mn A-site co-doping on the phase structure, defect chemistry, microstructure, electrical properties and device performance was systematically clarified. The main conclusions are as follows:

1) Moderate Li/Mn co-doping not only stabilizes the KBT main phase and reduces the $Bi_{1.74}Ti_2O_{6.624}$ impurity phase but also enhances in-plane lattice anisotropy, TiO_6 octahedral distortion, and the coupling between $[Bi_2O_2]^{2+}$ layers and perovskite-like blocks, thereby improving the structural integrity and high-temperature reliability of the material.

2) Li/Mn co-doping induces a transition in dielectric behavior from a sharp λ-type anomaly to a diffuse or relaxor-like response, with both γ and T_C gradually increasing as the doping concentration increases. High-temperature ferroelectric hysteresis tests further confirm that the material achieves balanced control of conduction suppression and domain-wall mobility. AC impedance analysis shows that this doping strategy effectively suppresses leakage conduction and improves high-temperature insulation performance.

3) KBT–LM55 ceramics exhibit the maximum crystal distortion and optimal ferroelectric performance, with a d_{33} of 30 pC/N, a T_C of 590 °C, and a tanδ as low as 0.23%. After annealing at 500 °C for 4 h, its d_{33} remains at 80% of the initial value. Resonance tests further demonstrate that the sample possesses excellent intrinsic thermal stability, with k_p remaining stable up to 325 °C.

4) An ultrasonic pulse–echo transducer using KBT–LM55 ceramics maintains stable signals up to 250 °C, with an f_c of 2.24 MHz, a $BW_{-6\ dB}$ of 33.95%, and a V_{p-p} of 1.94 V. Energy attenuation at high temperatures is primarily due to thermally enhanced damping and medium-related losses, not intrinsic material degradation.

Acknowledgements

This work was funded by the National Natural Science Foundation of China (No. 12372179).

Availability of data and materials

The data that support the findings of this study are available from the corresponding author upon reasonable request.

Competing interests

The authors have no competing interests to declare that are relevant to the content of this article.

References

[1] Zhang TD, Yang LY, Zhang CH, *et al.* Polymer dielectric films exhibiting superior high-temperature capacitive performance by utilizing an inorganic insulation interlayer. *Mater Horiz* 2022, **9**: 1273–1282.

[2] Cai JH, Qi JL, Yang YY, *et al.* Colossal permittivity and ultralow dielectric loss in Nb-doped $SrTiO_3$ ceramics. *J Adv Ceram* 2023, **12**: 2247–2256.

[3] Khan RU, Khan I, Ali B, *et al.* Structural, dielectric, optical, and electrochemical performance of $Li_4Mo_5O_{17}$ for ULTCC applications. *Mater Res Bull* 2023, **160**: 112142.

[4] Gu W, Yang B, Li DF, *et al.* Accelerated design of lead-free high-performance piezoelectric ceramics with high accuracy via machine learning. *J Adv Ceram* 2023, **12**: 1389–1405.

[5] Zhen LY, Lu LJ, Yao YT, *et al.* Flexible inorganic piezoelectric functional films and their applications. *J Adv Ceram* 2023, **12**: 433–462.

[6] Lee H, Zhang SJ, Bar-Cohen Y, *et al.* High temperature, high power piezoelectric composite transducers. *Sensors* 2014, **14**: 14526–14552.

[7] Yang AH, Huan Y, Wang QY, *et al.* Excellent comprehensive piezoelectric performances of SiC-doped BCTZ-based lead-free piezoelectric ceramics. *J Adv Ceram* 2025, **14**: 9221054.

[8] Luo BC, Feng W, Dai SW, *et al.* Stabilizing oxygen vacancies and promoting electrostrain in lead-free potassium niobate-based piezoelectrics over wide temperature ranges. *J Adv Ceram* 2024, **13**: 1965–1973.

[9] Liu H, Hao YJ, Yang ZQ, *et al.* Exceptional electrostrain with minimal hysteresis and superior temperature stability under low electric field in KNN-based lead-free piezoceramics. *J Adv Ceram* 2024, **13**: 364–372.

[10] Chen XY, Ou B, Liu GF, *et al.* Simultaneous enhancement of piezoelectric performance and Curie temperature in high-temperature $Bi_4Ti_3O_{12}$ piezoceramics through A/B site co-doping. *J Adv Ceram* 2025, **14**: 9221077.

[11] Abdulmajeed IM, Ibraheem SH. Effect of sintering temperature on the structural properties for $CaBi_4Ti_4O_{15}$ compound. *J Ovonic Res* 2022, **18**: 499.

[12] Chen XY, Ma ZQ, Li B, *et al.* Enhanced piezoelectric performance of Cr/Ta non-equivalent co-doped $Bi_4Ti_3O_{12}$-based high-temperature piezoceramics. *J Adv Ceram* 2024, **13**: 263–271.

[13] Xu JG, Xie SX, Xu Q, *et al.* Significantly enhanced performance and conductivity mechanism in Nb/Mn co-doped $CaBi_4Ti_4O_{15}$ ferroelectrics. *J Materiomics* 2024, **10**: 652–669.

[14] Luo XG, Yan ZN, Luo H, *et al.* Greatly improved piezoelectricity and thermal stability of (Na, Sm) co-doped $CaBi_2Nb_2O_9$ ceramics. *Adv Powder Mater* 2023, **2**: 100116.

[15] Zhang XL, Sun SM, Yin C, *et al.* Giant recoverable energy storage density for lead-free $SrTiO_3$-based dielectric films coated by the amorphous Al_2O_3 insulating layers. *J Adv Ceram* 2025, **14**: 9221175.

[16] Subbarao EC. A family of ferroelectric bismuth compounds. *J Phys Chem Solids* 1962, **23**: 665–676.

[17] Subbarao EC. Crystal chemistry of mixed bismuth oxides with layer-type structure. *J Am Ceram Soc* 1962, **45**: 166–169.

[18] Wang CM, Wang JF. Aurivillius phase potassium bismuth titanate: $K_{0.5}Bi_{4.5}Ti_4O_{15}$. *J Am Ceram Soc* 2008, **91**: 918–923.

[19] Wang CM, Wang JF, Mao CL, *et al.* Enhanced dielectric and piezoelectric properties of Aurivillius-type potassium bismuth titanate ceramics by cerium modification. *J Am Ceram Soc* 2008, **91**: 3094–3097.

[20] Guo ZL, Wang CM, Zhao TL, *et al.* Piezoelectric properties and thermal stabilities of cobalt-modified potassium bismuth titanate. *Mater Chem Phys* 2013, **140**: 260–265.

[21] Wang CM, Wang JF, Zhang SJ, *et al.* Electromechanical properties of A-site (LiCe)-modified sodium bismuth titanate ($Na_{0.5}Bi_{4.5}Ti_4O_{15}$) piezoelectric ceramics at elevated temperature. *J Appl Phys* 2009, **105**: 094110.

[22] Xi JW, Xing J, Chen H, *et al.* Crystal structure and electrical properties of Li/Mn co-doped NBT-based Aurivillius-type ceramics. *J Alloy Compd* 2021, **868**: 159216.

[23] Qin L, Jiang CB, Liu KH, *et al.* Structural and electric properties of Ce-doped $Na_{0.5}Bi_{4.5}Ti_4O_{15}$ piezoceramics with high Curie temperatures. *J Am Ceram Soc* 2020, **103**: 4083–4089.

[24] Chen Y, Zhang CC, Qin L, *et al.* Enhanced dielectric and piezoelectric properties in $Na_{0.5}Bi_{4.5}Ti_4O_{15}$ ceramics with Pr-doping. *Ceram Int* 2018, **44**: 18264–18270.

[25] Gai ZG, Wang JF, Zhao ML, *et al.* The effect of (Li,Ce) doping in Aurivillius phase material $Na_{0.25}K_{0.25}Bi_{4.5}Ti_4O_{15}$. *Scripta Mater* 2008, **59**: 115–118.

[26] Cummins SE, Cross LE. Electrical and optical properties of ferroelectric $Bi_4Ti_3O_{12}$ single crystals. *J Appl Phys* 1968, **39**: 2268–2274.

[27] Yi ZG, Wang Y, Li YX, *et al.* Ferroelectricity in intergrowth Bi_3TiNbO_9–$Bi_4Ti_3O_{12}$ ceramics. *J Appl Phys* 2006, **99**: 114101.

[28] Miyayama M, Yi IS. Electrical anisotropy in single crystals of bi-layer structured ferroelectrics. *Ceram Int* 2000, **26**: 529–533.

[29] Hu ZM, Koval V, Zhang HF, *et al.* Enhanced piezoelectricity in Na and Ce co-doped $CaBi_4Ti_4O_{15}$ ceramics for high-temperature applications. *J Adv Ceram* 2023, **12**: 1331–1344.

[30] Reddy SR, Prasad VVB, Bysakh S, *et al.* Superior energy storage performance and fatigue resistance in ferroelectric BCZT thin films grown in an oxygen-rich atmosphere. *J Mater Chem C* 2019, **7**: 7073–7082.

[31] Jaim HMI, Lee S, Zhang XH, *et al.* Stability of the oxygen vacancy induced conductivity in $BaSnO_3$ thin films on $SrTiO_3$. *Appl Phys Lett* 2017, **111**: 172102.

[32] Slouka C, Kainz T, Navickas E, *et al.* The effect of acceptor and donor doping on oxygen vacancy concentrations in lead zirconate titanate (PZT). *Materials* 2016, **9**: 945.

[33] Li GJ, Deng Y, Li T, *et al.* Efficient photocatalytic NO oxidation over novel NiAl layered double hydroxide/$Bi_4Ti_3O_{12}$ Z-scheme heterojunctions with boosted charge separation and O_2 activation. *J Mater Chem A* 2023, **11**: 13640–13652.

[34] Xiao P, Zheng QJ, Tian MJ, *et al.* Enhanced ferroelectricity/piezoelectricity, bright blue/yellow emission and excellent thermal stability in $Ca_{1-x}(LiDy)_{x/2}Bi_4Ti_4O_{15}$ lead-free multifunctional ceramics. *RSC Adv* 2016, **6**: 16387–16394.

[35] Wang YY, Zheng DY, Zheng XS, *et al.* Oxygen vacancies and electrical properties of different valence ions (W^{6+}, Nb^{5+}, Zr^{4+}, Cr^{3+}) doped $Bi_4Ti_3O_{12}$ ceramics. *Ceram Int* 2024, **50**: 2778–2787.

[36] Hu H, Jiang XP, Chen C, *et al.* Conduction and relaxation mechanism of $Na_{0.5}Bi_{8.5}Ti_7O_{27}$ inter-growth bismuth layer-structured piezoelectric ceramics. *J Ceram* 2020, **41**: 171–177. (in Chinese)

[37] Jovalekić Č, Zdujić M, Atanasoska L. Surface analysis of bismuth titanate by Auger and X-ray photoelectron spectroscopy. *J Alloy Compd* 2009, **469**: 441–444.

[38] Zhou ZY, Dong XL, Huang SM, *et al.* Dielectric relaxation of La^{3+}-modified Bi_3TiNbO_9 Aurivillius phase ceramics. *J Am Ceram Soc* 2006, **89**: 2939–2942.

[39] Chen Y, Xu JG, Xie SX, *et al.* Ion doping effects on the lattice distortion and interlayer mismatch of Aurivillius-type bismuth titanate compounds. *Materials* 2018, **11**: 821.

[40] Abdul-latif A, Nagib O. Diffuseness parameter as a bottleneck for accurate half-life calculations. *Phys Rev C* 2019, **100**: 024601.

[41] Rehman F, Jin H B, Li J B. Effect of reduction/oxidation annealing on the dielectric relaxation and electrical properties of Aurivillius $Na_{0.5}Gd_{0.5}Bi_4Ti_4O_{15}$ ceramics. *RSC Adv.* 2016, **6**: 35102–35109.

[42] Zhang HT, Yan HX, Reece MJ. Microstructure and electrical properties of Aurivillius phase $(CaBi_2Nb_2O_9)_{1-x}(BaBi_2Nb_2O_9)_x$ solid solution. *J Appl Phys* 2010, **108**: 014109.

[43] Abrahams SC, Kurtz SK, Jamieson PB. Atomic displacement relationship to Curie temperature and spontaneous polarization in displacive ferroelectrics. *Phys Rev* 1968, **172**: 551–553.

[44] Aoyagi R, Takeda H, Okamura S, *et al*. Ferroelectric and piezoelectric properties of bismuth layered-structure ferroelectric (Sr,Na,Bi) $Bi_2Ta_2O_9$ ceramics. *Mater Sci Eng B—Adv* 2005, **116**: 156–160.
[45] Merz WJ. Double hysteresis loop of $BaTiO_3$ at the Curie point. *Phys Rev* 1953, **91**: 513–517.
[46] Martirena HT, Burfoot JC. Grain-size and pressure effects on the dielectric and piezoelectric properties of hot-pressed PZT-5. *Ferroelectrics* 1974, **7**: 151–152.
[47] Vogel DH. The law of the temperature dependence of the viscosity of liquids. *Phys Z* 1921, **22**: 645–646.
[48] Fulcher GS. Analysis of recent measurements of the viscosity of glasses. *J Am Ceram Soc* 1925, **8**: 339–355.
[49] Tammann G, Hesse W. The dependence of viscosity on temperature in supercooled liquids. *Z Anorg Allg Chem* 1926, **156**: 245–257. (in German)
[50] Tagantsev AK. Vogel–Fulcher relationship for the dielectric permittivity of relaxor ferroelectrics. *Phys Rev Lett* 1994, **72**: 1100–1103.
[51] Pirc R, Blinc R. Vogel–Fulcher freezing in relaxor ferroelectrics. *Phys Rev B* 2007, **76**: 020101.
[52] Blake SM, Falconer MJ, McCreedy M, *et al*. Cation disorder in ferroelectric Aurivillius phases of the type $Bi_2ANb_2O_9$ (A = Ba, Sr, Ca). *J Mater Chem* 1997, **7**: 1609–1613.
[53] Shannon RD. Revised effective ionic radii and systematic studies of interatomic distances in halides and chalcogenides. Acta Crystallogr A 1976, 32: 751–767.
[54] Zhao Z, Buscaglia V, Viviani M, *et al*. Grain-size effects on the ferroelectric behavior of dense nanocrystalline $BaTiO_3$ ceramics. *Phys Rev B* 2004, **70**: 024107.
[55] Woodward PM. Octahedral tilting in perovskites. I. geometrical considerations. *Acta Crystallogr B* 1997, **53**: 32–43.
[56] Benedek NA, Rondinelli JM, Djani H, *et al*. Understanding ferroelectricity in layered perovskites: New ideas and insights from theory and experiments. *Dalton T* 2015, **44**: 10543–10558.
[57] Sun SJ, Yin XF. Progress and perspectives on Aurivillius-type layered ferroelectric oxides in binary $Bi_4Ti_3O_{12}$–$BiFeO_3$ system for multifunctional applications. *Crystals* 2021, **11**: 23.
[58] Zhang HT, Yan HX, Reece MJ. The effect of Nd substitution on the electrical properties of Bi_3NbTiO_9 Aurivillius phase ceramics. *J Appl Phys* 2009, **106**: 044106.
[59] Li W, Chen AP, Lu XM, *et al*. Collective domain-wall pinning of oxygen vacancies in bismuth titanate ceramics. *J Appl Phys* 2005, **98**: 024109.
[60] Nayak P, Badapanda T, Singh AK, *et al*. Possible relaxation and conduction mechanism in W^{6+} doped $SrBi_4Ti_4O_{15}$ ceramic. *Ceram Int* 2017, **43**: 4527–4535.
[61] Chen Y, Zhou Z, Li LF, *et al*. Synergistically enhancing the piezoelectric activity and Curie temperature of $CaBi_4Ti_4O_{15}$ ceramics via co-doping Gd/Mn at the A/B-site. *J Adv Ceram* 2024, **13**: 1482–1497.
[62] Cheng YT, Guan SY, Wang Q, *et al*. Mechanism and application of lead-free KNN-based ceramics with superior piezoelectricity. *J Eur Ceram Soc* 2024, **44**: 6978–6986.
[63] Kazys R, Vaskeliene V. High temperature ultrasonic transducers: A review. *Sensors-Basel* 2021, **21**: 3200.
[64] Oppenheim AV, Schafer RW, Buck JR. *Discrete-Time Signal Processing*. New Jersey (USA): Prentice-Hall, Inc.,1999.
[65] Kinsler LE, Frey AR, Coppens AB, Sanders JV. *Fundamentals of Acoustics*. New York (USA): John Wiley & Sons, 2000.
[66] Moure A, Alemany C, Pardo L. Temperature dependence of piezoelectric, elastic and dielectric coefficients at radial resonance of piezoceramics with an Aurivillius-type structure. *IEEE T Ultrason Ferr* 2005, **52**: 570–577.